

The Astrophysical Journal, submitted

***Spitzer* Infrared Spectrograph Observations of Magellanic Cloud
Planetary Nebulae: the nature of dust in low metallicity
circumstellar ejecta¹**

Letizia Stanghellini

National Optical Astronomy Observatory, 950 N. Cherry Av., Tucson, AZ 85719

lstanghellini@noao.edu

Pedro García-Lario

*Herschel Science Centre, European Space Astronomy Centre, Research and Scientific
Support Department of ESA, Villafranca del Castillo, P.O. Box 50727. E-28080 Madrid,
Spain*

Pedro.Garcia-Lario@sciops.esa.int

D. Anibal García-Hernández

*The W. J. McDonald Observatory. The University of Texas at Austin, 1 University Station
C1402, Austin, TX 78712*

agarcia@astro.as.utexas.edu

Jose V. Perea-Calderón

European Space Astronomy Centre, INSA S. A., P.O. Box 50727. E-28080 Madrid, Spain

Jose.Perea@sciops.esa.int

James E. Davies

National Optical Astronomy Observatory, 950 N. Cherry Av., Tucson, AZ 85719

jdavies@noao.edu

Arturo Manchado

*Instituto de Astrofísica de Canarias, vía Láctea s/n, La Laguna, E-38200 Tenerife, Spain;
affiliated to CSIC, Spain*

amt@iac.es

Eva Villaver

*Space Telescope Science Institute, 3700 San Martin Drive, Baltimore MD 21218; affiliated
to the Hubble Space Telescope Department of ESA*

villaver@stsci.edu

Richard A. Shaw

National Optical Astronomy Observatory, 950 N. Cherry Av., Tucson, AZ 85719

shaw@noao.edu

ABSTRACT

We present 5–40 μm spectroscopy of 41 planetary nebulae (PNe) in the Magellanic Clouds, observed with the Infrared Spectrograph on board the *Spitzer Space Telescope*. The spectra show the presence of a combination of nebular emission lines and solid-state features from dust, superimposed on the thermal IR continuum.

By analyzing the 25 LMC and 16 SMC PNe in our sample we found that the IR spectra of 14 LMC and 4 SMC PNe are dominated by nebular emission lines, while the other spectra show solid-state features. We observed that the solid-state features are compatible with carbon-rich dust grains (SiC, polycyclic aromatic hydrocarbons (PAHs), etc.) in most cases, except in three PNe showing oxygen-rich dust features. The frequency of carbonaceous dust features is generally higher in LMC than in SMC PNe.

The spectral analysis allowed the correlations of the dust characteristics with the gas composition and morphology, and the properties of the central stars. We found that: 1) all PNe with carbonaceous dust features have $\text{C/O} > 1$, none of these being bipolar or otherwise highly asymmetric; 2) all PNe with oxygen-rich dust features have $\text{C/O} < 1$, with probable high mass progenitors if derived from single-star evolution (these PNe are either bipolar or highly asymmetric); 3) the dust temperature tracks the nebular and stellar evolution; and 4) the dust production efficiency depends on metallicity, with low metallicity environments not favoring dust production.

¹based on observations made with the *Spitzer Space Telescope*, which is operated by the Jet Propulsion Laboratory, California Institute of Technology, under a contract with NASA.

Subject headings: Planetary nebulae; Magellanic Clouds; Dust; solid state features; morphology

1. Introduction

Planetary nebulae (PNe) are the envelopes ejected toward the end of the evolution of low- and intermediate-mass stars ($1\text{--}8\text{ M}_{\odot}$), at the tip of the thermally pulsing asymptotic giant branch (TP-AGB) phase. The gas and dust ejected in this phase contain elements that had been produced by nucleosynthesis and then carried to the stellar surface by convective dredge-up processes. The slow wind that eventually produces the PN, also called the superwind, starts with the AGB thermal pulses and carries most of the envelope mass during the last few thermal pulses (Vassiliadis & Wood 1993). The composition of the ejecta is tightly correlated to the initial mass and metallicity of the evolving star: higher masses in this range will have undergone hot bottom burning (HBB) nucleosynthesis, which depletes carbon and increases nitrogen in PNe (e.g., Marigo 2001). The exact mass-loss mechanism and superwind onset are unclear to date, and, most importantly, their dependence on the mass and metallicity of the stellar progenitor is unconstrained.

Dust is formed on the cool surface of the AGB star, and radiation pressure on the dust grains may be a dominant factor in the superwind onset. Furthermore, the nature of the dust grains affects dust opacity, thus the role of dust grains in the superwind efficiency must be related to the chemistry of the nebula. Interestingly, Willson (2000) showed that mass loss might also occur in the absence of dust.

A PN is born when the circumstellar matter ejected during the superwind phase is ionized by the UV flux from the central star. Dust in PNe survives the sputtering due to the UV radiation field for a time period that depends on the nature of the dust grains, rather than on the expansion rate and the luminosity of the central star (e.g., Kaeufl et al. 1993). Dust in Galactic PNe has been observed extensively. It has been shown that about 40% of the emergent bolometric flux in Galactic PNe occurs between 5 and 60 μm (Zhang & Kwok 1991) in the form of a blackbody-like continuum spectrum due to dust scattering (Cohen & Barlow 1974). Dust in Galactic PNe has been characterized by its cool (100–200 K) temperature, producing a spectrum peaking at 25–60 μm . The physical extent of the dust coincides with the gas emission in most nebulae and is even more extended in others (Volk 2003).

Observations of AGB stars and PNe in the Galaxy and the Large (LMC) and Small (SMC) Magellanic Clouds, and other Local Group galaxies provide increasing evidence that

metallicity may play a role in the AGB and beyond (i. e., García-Hernández et al. 2007). On average, the LMC and SMC metallicities are respectively $\sim 50\%$ and 25% that of the Galaxy (Caputo et al. 1999). The absence of heavily obscured AGB stars in the Magellanic Clouds (Groenewegen et al. 2000; Trams et al. 1999), in contrast with their Galactic counterparts, suggests that, on average, lower metallicity environments are less favorable to dust production. The ratio of carbon-rich to oxygen-rich AGB stars in Local Group galaxies decreases with increasing metallicity (Cioni & Habing 2003; Cioni et al. 2003; Schultheis et al. 2004). AGB stars in low-metallicity galaxies would take a long time to lose their envelopes if the mass-loss efficiency was proportional to dust content. Their lifetime as AGB stars could be very long, increasing the chance of the nuclear-processed material to surface in their lifetime. In this way, a higher concentration of nuclear-reaction products is explained. In contrast, high-metal stars would have powerful dust-driven mass-loss rates. As a consequence, their chemistry will be less affected. Stanghellini et al. (2003) analyzed all Magellanic Cloud PNe that have been previously observed with the *HST* cameras and found that the frequency of asymmetric (e. g., bipolar, quadrupolar) PNe in the SMC is only 60% that of the LMC, where the metallicity is, on average, higher. One may infer that bipolar morphology is less favorable in the low-metal environment of the SMC than in the LMC and the Galaxy. Aspherical PNe, especially the bipolar ones, are typically more massive than their spherical counterparts, indicating a more efficient mass-loss mechanism (Peimbert & Serrano 1980). Furthermore, the mere bipolar shape indicates the presence of a gas-dust torus around the central star, constraining the outflow into bipolar shape. It is no coincidence that the internal extinction of bipolar PNe is higher than that of spherical PNe. It occurred to us that the different morphologies may form with completely different mass-loss mechanisms, and that the low-metallicity, low-dust environments may produce only spherical PNe.

From the above described observing results, it is obvious that metallicity affects the properties of PNe, so that it becomes clear that the dust properties in PNe need to be studied in a variety of metallicity environments, and there is a good reason to observe dust features in relation to the absolute physical characteristics of the nebulae and stars. These are the scientific strands that motivated us to perform the IRS observations on the Magellanic Cloud PNe presented in this paper. While Galactic PNe have been studied with IRAS and ISO (Zhang & Kwok 1991, García-Lario & Perea Calderón 2003), most Magellanic Cloud PNe were beyond the reach of these IR telescopes. Magellanic Cloud PNe have known distances, thus lowering the number of free parameters in the comparison between the data and the models.

This paper presents low resolution IRS *Spitzer* spectra for 25 LMC and 16 SMC PNe. In §2 we present the observations relative to this data-set and the data analysis, including the spectral analysis and a description of individual nebulae. Section 3 presents the study of the

correlations between the dusty nature of the PNe and their gas morphology and evolution, §4 contains the discussion of our findings, and §5 summarizes our conclusions and suggests future endeavors in this field.

2. Observations and data analysis

2.1. Sample selection

Our goal is to study the infrared spectral properties of PNe in the Magellanic Clouds, and to relate them to morphology and other nebular properties, and to the nature of their central stars, in order to gain insight on their formation and evolution. In order to meet our science goals we have selected LMC and SMC PNe that satisfy the following selection: (1) All targets have been previously observed with the *HST* cameras (Shaw et al. 2001, 2006; Stanghellini et al. 1999, 2002), thus morphological (and, in many cases, stellar) information is available. (2) All targets are smaller than $2''$ in apparent size, to facilitate accurate peak-up observations. This requirement excludes only a very small fraction of Magellanic Cloud PNe that have been observed with *HST*. These restrictions do not exclude evolved PNe significantly: at the distance of the Magellanic Clouds, $2''$ implies a PN diameter between 0.5 pc (for the LMC) and 0.6 pc (for the SMC). Thus, for typical PN expansion velocities our sample includes PNe up to ~ 9000 yr after ejection (see models by Villaver et al. 2002), which is a substantial fraction of their visible lifetime. (3) The abundances of the elements that are related to AGB evolution and population (He, N, O, Ar, S) are available in the literature. (4) Carbon abundances have been measured from their UV spectra (Stanghellini et al. 2005, Leisy & Dennefeld 1996).

After filtering the Magellanic Cloud PNe sample through the above selection, we also excluded those targets already in the Reserved Observation Catalog (ROC) through the *Spitzer* GTO or other programs. We shall study those targets in the future through the *Spitzer* Data Archive. In Figure 1 we show the histogram of the [O III] $\lambda 5007$ flux distribution of all Magellanic Cloud PNe that satisfy selection rules (1) and (2) above. These include targets observed by us (black histogram), and those in the ROC (gray histogram). The sample presented in this paper is most representative of the [O III]-bright Magellanic Cloud PNe, where the [O III] $\lambda 5007$ brightness is a good proxy for the optical PN brightness for all but the most unevolved PNe (Stanghellini et al. 2002). However, there is increasing evidence for a significant population of very low excitation (VLE) PNe in both the LMC (Reid & Parker 2006b) and the SMC (Jacoby & De Marco 2002), where [O III] is very weak and the $F(\text{[N II]})/F(\text{H}\alpha)$ ratio can be very strong. While it is not clear that a sample selection based on [O III] brightness inherently selects against a particular population of

PNe, VLE nebulae may nevertheless be under-represented in our sample. Additional mid-IR spectra of VLE nebulae will be needed to understand the applicability of the results presented here to this class of PNe. In Table 1 we list the selected targets, with their angular radii and morphologies derived from the *HST* images (Shaw et al. 2001, 2006; Stanghellini et al. 1999, 2002).

2.2. Spitzer Observations

The spectral data were acquired with the Infrared Spectrograph (IRS, Houck et al. 2004) on board the *Spitzer Space Telescope* (Werner et al. 2004) between 2005 July 14 and November 14 as part of a General Observer program (#20443). The observing log is given in Table 2, where we list the target name, the coordinates from the *HST* images, the observing date, the dataset ID number, and the observing campaign. The 5–40 μm range spectra were acquired by using the Spitzer 5.2–8.7 μm Short Low 2nd order (SL2), the 7.4–14.5 μm Short Low 1st order (SL1), the 14.0–21.3 μm Long Low 2nd order (LL2), and the 19.5–38.0 μm Long Low 1st order (LL1) IRS modes. Each of the observations consists of 3 cycles of 14 sec and 30 sec duration each for the SL and LL segments respectively. We also performed peak-up on a nearby star to achieve accurate (0.4") pointing. We obtained spectra of 41 PNe. The target SMP LMC 30, originally on our target list, was not pointed accurately enough for spectral extraction.

The data were first processed by the *Spitzer Science Center* (SSC) using the standard data reduction pipeline version 12.4 (except for one source, SMP LMC 100, which was processed by the pipeline version 13, which was suitable for this dataset). This process includes the linearization correction, the subtraction of darks, and cosmic ray removal. The images were also corrected for stray light, and a flat-field correction was applied to account for pixel-to-pixel response variations. Through the IRS data reduction pipeline we obtained three Basic Calibrated Data (BCD) files for each slit nod position. These three cycles were then combined by the pipeline using a signal-weighted average to produce the co-added 2-D images.

The pipeline-processed 2-D images were further cleaned by interpolating over the flagged data and rogue pixels, which depend on the observation campaign. Sky background was removed by using the image degeneracy relative to the two nod positions. Spectral extraction, and wavelength and flux calibration were performed with the *Spitzer IRS Custom Extractor* (SPICE), with point source aperture. The resulting 1-D spectra were cleaned for bad pixels, spurious jumps and glitches, smoothed and merged into one final spectrum per module for

each source using the IRS Spectroscopy Modeling Analysis and Reduction Tool (SMART¹). The overlap regions between orders in the four modules were masked by hand to produce a smooth, artifact-free spectrum in the 5.2–38 μm range. The third *bonus* order contributed by the SL and LL modules were also masked, so in the end, each PN has two spectra, one for each nod position.

2.3. Spectral analysis

The infrared emission from the target PNe is composed of one or more of the following components: narrow emission lines from collisionally excited atomic species (nebular lines), thermal continuum emission, and emission from dust grains. Most of our IRS spectra show continuum emission at different brightness levels, and nebular emission lines and solid state features superimposed on the continuum. We analyzed each of these components in turn.

We identified and measured the nebular lines in the PN spectra by using the line-fitting routine in SMART. A single-order fit was made to the baseline for each nebular line, and the line was then fitted using a single Gaussian. The measured line strengths and widths will be presented in a future paper, together with a detailed nebular analysis. We found a spurious feature in the spectrum, nominally at 19 μm , whose detection was possible due to its slight offset between nodding positions. In some cases it falls very close to the [S III] line at 18.7 μm , and in these cases the feature was removed before the measurement of the [S III] line. From an inventory of the nebular emission lines in the IRS wavelength range we defined four major excitation classes. We designate the PNe to be low excitation if only the [S III] lines are visible, intermediate excitation when the spectra shows [Ar III], [S IV], and [Ne III] nebular emission, high excitation if we also detect [O IV], and very high excitation if we also see the [Ne IV] or [Ne V] emission. Several PNe show both low and high excitation lines, likely due to different excitation zones in the nebulae.

In order to study the emission from the dust, a single blackbody was fitted to the merged cleaned continuum using data from both nod positions. Nebular lines and solid-state features were masked during the fitting procedure to isolate the continuum. Data with $\lambda > 38\mu\text{m}$ in the LL1 module were often masked as well due to the increased noise at these wavelengths. Figures 2 through 5 show the best fit Black-body curves to the data, which are adopted as the continuum fits, and the continuum-subtracted spectra in four PNe representing a variety of IRS spectral features. The top panels show, for each nod position,

¹SMART was developed by the IRS Team at Cornell University and is available through the *Spitzer Science Center* at Caltech.

the original spectra and the Black-body fit (indicated by a thicker line); the bottom panel shows the continuum-subtracted spectra and includes the emission line identifications. Solid-state features were measured using an IDL routine developed by us which allows for varying the start and end-points of the feature to be fitted. Solid-state fits were performed on the continuum-subtracted spectra.

All the IRS spectra show evidence of a thermal continuum with superimposed nebular emission lines. In addition, the presence of solid-state emission features are superimposed on some of the spectra. We sort the PNe into three different IRS spectral types: F, CRD, and ORD types. We define as F (for featureless) those PNe that show no evidence of solid-state features. The lack of features is due either to the actual absence of grain emission, such as may be expected in evolved PNe, or to the dust features possibly being below the detection limit. In this class, we include the objects that show possible but not certain dust emission features. CRD (for carbon-rich dust) PNe are those whose spectra show carbon-rich dust features. This class includes multiple types of dust grains. Among CRD we find spectra showing the very broad $11\ \mu\text{m}$ emission of silicon carbide, other spectra showing broad peaks at 6-9, 11-15, and 15-21 μm generally attributed to very small carbonaceous grains, possibly formed by large PAH clusters. PNe with evidence of the classic PAH emission features at 3.3, 6.2, 7.7, 8.6, and/or 11.3 μm are classified as CRD. Some CRD PNe show both broad and narrow carbon-rich dust features, superimposed, as if the ionized PAH features were beginning to form out of the clusters of small carbonaceous grains as evolution proceeds. ORD (for oxygen-rich dust) PNe are those whose spectra show oxygen-rich dust emission features, such as crystalline silicates.

In Figures 6 through 8 we show all the observed IRS spectra. Figures 6a, 6b, and 6c include all F PNe (listed alphabetically, the LMC PNe first). Figures 7a, 7b, and 7c show the CRD PNe. In Figures 7a through 7c we order the PNe by the strengths of the carbonaceous dust features, as they generally are thought to evolve in PNe. The sequence shows the evolution of certain features, but it is not an evolutionary sequence since PNe belong to different mass and/or metallicity sequences. Figure 8 shows the small sample of ORD PNe, where PNe have been ordered according to the strength of the degree of processing of their silicate features. All spectra show the two nod positions averaged. In Figures 7 and 8 these averages were normalized with respect to the flux at $14\ \mu\text{m}$, a feature-free region of all spectra.

In Table 3 we summarize the results from the analysis of the IRS spectra. In column (2) we give the dust temperature of the continuum, fitted as a black body; column (3) gives the infrared flux derived from the integration of the continuum dust spectra between 5 and 40 μm ; column (4) gives the IR excess; column (5) gives their dust type; and column (6)

gives the excitation class of the PN, based on the observed emission lines. From Montecarlo simulation based on several fits for the continua we infer that the fitting errors are below $\sim 5\%$ both in temperatures and IR fluxes. To obtain the ratios in column (4) we have used the Balmer line fluxes of these PNe from Stanghellini et al. (2002, 2003), and Shaw et al. (2006).

Below we list the general characteristics of the observed PNe. The dust type, based on the infrared spectrum for each target, is included.

SMP LMC 4 (Fig. 6a, F): With a low continuum level, the spectrum of this PN is regular and does not show solid-state features with the exception of very faint emission at $11.3\ \mu\text{m}$, which could be of interstellar nature, or the remnant of evaporated dust. The spectrum is almost featureless, but its classification based on solid-state features is uncertain. The nebular emission lines are characteristic of a very high excitation spectrum.

SMP LMC 9 (Fig. 7b, CRD): This spectrum shows faint emission at $11.3\ \mu\text{m}$, which is likely to be from PAHs. A host of nebular emission lines show a very high excitation nebula by the presence of [Ne V] at $24.2\ \mu\text{m}$.

SMP LMC 10 (Fig. 6a, F): A featureless spectrum apart from the nebular emission lines, including high excitation ones.

SMP LMC 16 (Fig. 6a, F): The line at about $9.8\ \mu\text{m}$ could be molecular hydrogen at $\lambda 9.66\ \mu\text{m}$, which is in contrast with the very high excitation nebular lines.

SMP LMC 18 (Fig. 6a, F): Faint and featureless, with the exception of a possible broad dust feature at $30\ \mu\text{m}$. The spectrum shows intermediate excitation nebular lines. Its classification based on dust features is uncertain due to a possible very low detection of the $15\text{--}20\ \mu\text{m}$ broad feature.

SMP LMC 19 (Fig. 7b, CRD): The feature at $11.3\ \mu\text{m}$ is likely to be narrow PAH emission. The emission spectrum indicates very high excitation.

SMP LMC 20 (Fig. 6a, F): As in the spectrum of SMP LMC 16, we are possibly detecting molecular hydrogen at $9.66\ \mu\text{m}$. Again, as in SMP LMC 16, the nebular lines denote a very high excitation PN, thus the molecular line is rather improbable.

SMP LMC 21 (Fig. 8, ORD): This PN has a unique spectrum that shows strong crystalline silicate emission. The nebular emission line spectrum is also interesting, showing a combination of low (i.e., [S III]) excitation nebular emission lines with very high excitation ones (i.e., [Ne VI]).

SMP LMC 25 (Fig. 7a, CRD): This spectrum shows carbon-rich dust features, which are

likely due to PAH clusters, or very small carbonaceous grains. We observe peaks at 6.2, 7.7, and 8.5 μm , all likely to be proto-PAH features, and a huge SiC emission at 11.3 μm . This is an intermediate excitation nebula.

SMP LMC 27 (Fig. 6a, F): This is an intermediate excitation nebula with no dust features, with the possible exception of the 30 μm broad feature as in SMP LMC 18.

SMP LMC 34 (Fig. 6b, F): An almost featureless spectrum, except for the nebular emission lines typical of intermediate excitation, and the solid-state feature at 30 μm , as in SMP LMC 18. It is hard to classify it based on solid-state features.

SMP LMC 45 (Fig. 6b, F): The nebular spectrum shows low to high excitation features, while the solid-state features are missing with the possible exception of the 30 μm feature.

SMP LMC 46 (Fig. 7b, CRD): The features at 7.9 μm and 11.3 μm could be PAHs or PAH-related, but very faint. The nebula has intermediate to high excitation.

SMP LMC 48 (Fig. 7a, CRD): The spectrum shows several complex solid state features. The broad feature at 6–9 μm , possibly due to small grain clusters, is superimposed on narrow features at 6.2, 7.7, and 8.6 μm , characteristic of PAHs. Other features are also seen at 15–20 μm and 30 μm . The PN is of intermediate excitation from the nebular lines.

SMP LMC 66 (Fig. 6b, F): In this nebula it is most apparent that the feature at 29.6 μm is an artifact, since it only appears in one of the nodding positions. This is a high excitation nebula with no solid state features in the spectrum.

SMP LMC 71 (Fig. 7c, CRD): This is a very high excitation spectrum with a solid state feature at 6.2 to 8.6 μm , possibly due to small grain clusters, superimposed on narrow features at 6.2, 7.7, and 8.6 μm , characteristic of PAHs. Other features are also seen at 15–20 μm and 30 μm .

SMP LMC 72 (Fig. 6b, F): This is a very high excitation spectrum without solid-state features.

SMP LMC 79 (Fig. 7c, CRD): Very interesting PAH features are present at 6.2, 7.7, 8.6, 11.3, and 13.5 μm , superimposed on broad features. Spectral lines are characteristic of a high excitation PN.

SMP LMC 80 (Fig. 6b, F): Dust featureless spectrum with intermediate excitation emission lines. The thermal continuum is undetected in this PN.

SMP LMC 81 (Fig. 8, ORD): The spectrum presents evident silicate features (SiO) at 9–12.5 μm . The broad emission between 16 and 30 μm is probably due to dust continuum.

The nebular emission spectrum shows intermediate excitation lines.

SMP LMC 95 (Fig. 6b, F): This nebula shows a high excitation spectrum. Although almost featureless, the solid-state spectrum is characteristic of an evolved PN, with a possible faint PAH feature showing at $11.3\ \mu\text{m}$.

SMP LMC 97 (Fig. 6c, F): This is a very high excitation PN without solid state features, with the possible exception of the $30\mu\text{m}$ broad feature.

SMP LMC 99 (Fig. 7c, CRD): This object shows a very high excitation spectrum. The solid-state features are similar to those of SMP LMC 71, with narrow PAH emission features superimposed on the broad dust features, possibly due to clusters of small grains. The $30\mu\text{m}$ broad feature is evident in the spectrum.

SMP LMC 100 (Fig. 7c, CRD): A very high excitation PN, this spectrum shows broad PAH signature and the $11\text{--}15\ \mu\text{m}$ bump typical of unevolved carbon-rich dust.

SMP LMC 102 (Fig. 6c, F): There is a possible PAH detection in this otherwise featureless spectrum.

SMP SMC 2 (Fig. 7b, CRD): The spectrum of this very high excitation PN shows very likely PAH emission at $11.3\ \mu\text{m}$.

SMP SMC 5 (Fig. 7c, CRD): Several PAH features are seen in this PN, superimposed on broad carbon-rich dust emission peaking at $8, 11.3\ \mu\text{m}$. The nebular excitation is very high.

SMP SMC 8 (Fig. 6c, F): The spectrum is featureless from the viewpoint of solid-state compounds. The nebular excitation is intermediate.

SMP SMC 9 (Fig. 6c, F): The spectrum shows no features and no emission lines, and the two nod position do not have the same continuum level.

SMP SMC 13 (Fig. 7a, CRD): This intermediate excitation spectrum shows broad carbon-rich features with peaks around 8 and $12\ \mu\text{m}$, typical of carbon-rich unevolved dust grains, and the broad feature at $30\ \mu\text{m}$.

SMP SMC 14 (Fig. 7c, CRD): A high excitation PN, shows narrow PAH features with peaks at $6.2, 7.7, 8.6,$ and 11.3 , characteristic of PAH emission, superimposed on broad features.

SMP SMC 15 (Fig. 7a, CRD): The $[\text{S IV}] \lambda 10.5$ emission appears on top of the broad solid state feature. This nebula is an extremely good example of the emission expected from carbon-rich dust grains before they become PAHs. Note that the $15\text{--}21\ \mu\text{m}$ feature may be the precursor of the PAH feature that would be found at $17.0\text{--}17.7\ \mu\text{m}$. In addition, the

broad 30 μm feature is also clearly seen. This PN is an intermediate excitation one.

SMP SMC 16 (Fig. 7b, CRD): Broad carbon-rich dust features appear with peaks at 6–9 and 11–15 μm , typical of unprocessed clusters of small carbonaceous grains and/or large PAH clusters. This is a low excitation PN.

SMP SMC 17 (Fig. 7c, CRD): Similar to SMP SMC 16, but with PAH narrow peaks appearing at 6.2, 7.7, 8.7, and 11.3 μm . This is an intermediate excitation PN.

SMP SMC 18 (Fig. 7a, CRD): This is another very good example of the emission expected in a carbon-rich source with dust grains where PAHs have not yet been formed, showing broad SiC emission. Note the plateau features at 6–9 μm , 11–15 μm , and 15–21 μm , as well as the extremely broad 30 μm feature. The excitation for this nebula is intermediate.

SMP SMC 19 (Fig. 7c, CRD): Some carbon-rich dust features, both narrow PAH peaks and broad, unevolved ones, are present, together with very high excitation lines.

SMP SMC 20 (Fig. 7a, CRD): This source is similar to SMP SMC 15; with huge SiC features, it is probably the least evolved source among the PNe showing carbon-rich features.

SMP SMC 23 (Fig. 6c, F): This object has a featureless spectrum, apart from a couple of intermediate excitation emission lines.

SMP SMC 25 (Fig. 8, ORD): Unique source in the SMC showing oxygen-rich dust silicates peaking shortward of 11 μm . The solid state features are similar to those of SMP LMC 81, but with some crystalline silicates features arising over the continuum longward of 20 μm . This is a very high excitation nebular spectrum, high dust and effective temperature, and a very high central star mass PN.

SMP SMC 26 (Fig. 6c, F): The faint feature at 11.3 μm could be a PAH. The nebular spectrum shows very high excitation lines.

SMP SMC 27 (Fig. 7b, CRD): Intermediate excitation PN with carbon-rich dust emission of the broad type.

3. Correlations between IR spectral characteristics and other nebular and stellar properties

We studied the interrelations between the properties that we derived from the IRS spectra and the properties derived from other studies. We have specifically selected a target sample of PNe whose morphology, gaseous carbon abundance, and central stars have been studied through *HST* imaging and spectroscopy. The sizes of the PNe have been determined

from the angular size measured from *HST* images (see Table 1) and the distances to the Magellanic Clouds. In this paper we adopt $d_{\text{LMC}} = 50.6$ kpc (Freedman et al. 2001; Mould et al. 2000) and $d_{\text{SMC}} = 58.3$ kpc (Westerlund 1997), used also to get the IR luminosity in solar units from the fluxes of Table 3.

The PNe in our sample represent an assortment of initial masses and metallicities; they show a variety of morphological types and also represent a variety of evolutionary stages. Care is needed in disentangling the evolutionary effects on the physical quantities plotted and their intrinsic values, related to mass and metallicity.

Figure 9 shows the measured infrared luminosity versus carbon abundance (here the abundances are in terms of $\log X/H + 12$, where X is the element considered) of all PNe of our sample that have a carbon determination either from Leisy & Dennefeld (1996) or from Stanghellini et al. (2005). We estimated that the infrared luminosity errors are of the order of 5%; typical carbon abundance uncertainties are ~ 5 to 10%. This implies that errorbars in Figure 9 would be smaller or comparable to the sizes of the symbols used for the data points. The two parts of Figure 9 display PNe on the same plane, where dust type and morphology are identified by symbol type in the left and right panels respectively. The loci of the different dust type PNe are well separated in this plot: the PNe with featureless spectra (F), are typically at low to intermediate luminosity and present a spread in carbon abundances. The PNe with CRD spectra are on the upper right of the plot. PNe with oxygen-rich dust spectra, or ORD, are on the upper left of the plot. From the figure we infer a strong relation between the gas and dust composition: CRD IRS spectra are only found in carbon-rich PNe.

By comparing the left and right panels of Figure 9 we note that no bipolar, quadrupolar, or point-symmetric PNe (squares) in the figure correspond to PNe with carbonaceous dust. The carbon gas abundance, dust type, and morphology are thus very clearly interrelated. Since gaseous carbon is depleted in massive PN progenitors via the HBB reactions, in Figure 9 the progenitor mass of PNe decreases from left to right. PNe with high mass progenitors in the figure are ORD PNe if they are IR-bright; otherwise they are featureless. It is possible that some of the F PNe on the lower left of the plot are indeed evolved versions of the ORD PNe on the upper left. It is worth noting that the SMC PNe in the plot are restricted to the upper right part, with $\log C/H + 12 > 8.4$ and $\log L_{\text{IR}}/L_{\odot} > 1.9$.

More insight comes from Figure 10, where we plot the carbon vs. oxygen abundances (oxygen abundance uncertainties are similar or smaller than those for carbon, thus errorbars in Figure 10 are smaller than symbol size). Once again, the left and right panels identify dust type and morphology. The left panel shows that PNe with PAHs and other carbonaceous dust features all have $C/O > 1$, while $C/O < 1$ for all ORD PN, and there are no exceptions

to these correlations. The right panel of Figure 10 shows that all asymmetric PNe have low carbon abundance, and either oxygen-rich dust or no dust features. It is clear that PNe whose progenitors have gone through the HBB do not develop carbonaceous dust. We found that the average N/O for CRD PNe is ~ 0.3 , while it is ~ 2 for ORD PNe, a clear sign of HBB activity.

In Table 4 we summarize the group properties of the different dust types, separating the columns for the LMC and the SMC PNe. In this table, abundances (Stanghellini 2006) are reported linearly, in terms of hydrogen. In column 1 we give the diagnostics, and columns (2) through (7) give respectively their values (and standard deviation, in row 2 through 6) for the samples. Note that in a few cases we do not have data to fill the tables, and in those cases where we did not report the deviation we only have one datum for the diagnostics. It is worth mentioning that ORD PNe, those whose progenitors are likely more massive and which have gone through HBB nucleosynthesis, are not necessarily those with the higher oxygen abundances. This is a phenomenon that is especially marked in the Magellanic Cloud PNe, where the enhanced efficiency of the ON cycle at low metallicity depletes both carbon and oxygen in favor of nitrogen (Stanghellini 2006). This is also why the oxygen abundances are a poor indicator of PN metallicity for PNe whose progenitors have gone through the HBB.

In Figure 11 we show the dust temperature vs. physical radius of the nebulae (both quantities have uncertainties smaller than 0.02 dex). The straight line shows the best fit using all plotted data, and suggests a power-law decline of $T_{\text{dust}} \propto R^{-0.25}$. Once again, dust types are identified in the left panel, morphology in the right panel. The physical radii of these PNe are photometric radii (e.g., Shaw et al. 2001), and correspond to the geometrical radius of the ionized gas for all except the bipolar PNe with large lobes. Planetary nebulae with larger radii are generally more evolved than those with small radii, thus it is not surprising that the radii are inversely proportional to some power of the dust temperature. Lenzuni et al. (1989) showed a similar plot for Galactic PNe that were observed with the IRAS satellite and inferred that $T_{\text{dust}} \propto R^{-0.15}$. We confirm that the grain efficiency of PNe (within the same dust type) decreases with time, probably due to sputtering of material off the grain surface. It is also interesting to note that our much higher precision in the radius determination (because in Magellanic Cloud PNe, the distances are known and accurate angular sizes are available from the HST imagery) and the dust temperature (since temperature is derived from a spectral fit, and not by interpolation of a few photometric data points, as for the IRAS data for Galactic PNe) does not significantly decrease the scatter of the relation compared to the Galactic plot of Lenzuni et al. (1989); this suggests that the scatter is real and depends on the grain properties.

In Figure 12 we show the tight relation between the dust temperature and the IR

luminosity. PNe evolve from high to low dust temperatures, and from high to low IR luminosity, i.e., from the upper right to the lower left of the plots. All ORD PNe are at intermediate evolutionary stages. Uncertainties of the data points are smaller than 0.02 dex in both axes. At very low IR luminosity and temperatures, where the most evolved PNe are found, we only find F PNe.

The electron density of the gas is another parameter that decreases as the nebula evolves. This is studied in Figure 13, where the dust temperature and the electron density show a tight correlation. It is worth noting that the CRD PNe follow a tighter correlation than F and ORD PNe. It is also important to mention that dust temperature does not correlate with optical extinction. Typical errors in the logarithmic density scale are smaller than ~ 0.1 dex, while the dust temperature uncertainties are negligible in this scale.

While the anti-correlation of dust temperature with nebular radius indicates a general evolutionary trend, it is only by studying nebulae and their central stars together that one can disentangle the evolutionary effects from the effect of the mass of the PN progenitors and the final core mass of the central stars. In the HR diagram of Figure 14 we can characterize the evolution of post-AGB stars by mass bins, thus singling out the effects of evolution from those due to dynamical evolution and nebular acceleration.

In Figure 14 we show the loci of the central stars, of those PNe in our sample whose stellar physical parameters are available, on the $\log T_{\text{eff}} - \log L/L_{\odot}$ plane (individual effective temperature errors are negligible on the log scale (see Villaver et al. 2003, 2004, 2006), while luminosity uncertainties are typically of the order of 0.05 dex). The plot shows the evolutionary tracks of hydrogen-burning post-AGB stars with masses of 0.57, 0.6, 0.7, 0.75, and 0.9 M_{\odot} , taken from the models of Stanghellini & Renzini (2000). The symbols refer to the dust type (left panel) and morphological (right panel). We have plotted only stars whose luminosity has been measured directly, from their magnitudes, and have not included model-dependent luminosity determination (Villaver et al. 2003, 2004, 2006). We only used those stars whose effective temperatures have been evaluated via He II Zanstra analysis. From the figure we infer that the F and CRD PNe can be found around stars with a range of evolutionary stages and core masses, while the only ORD PNe whose location on the HR diagram is known correspond to a high mass evolutionary track.

In Figure 15 we show the sequence of CRD PNe with nebular size. All PNe whose spectra have been depicted in Figure 7 (a through b) have been assigned a sequence number, 1 to 20, as ordered in the Figure. The sequence starts with PNe featuring huge SiC (in order of strength), then goes to those PNe with broad and narrow carbonaceous features superimposed, then to the PAH feature PNe, and finally to those PNe with strong PAH emission. The symbols in Figure 15 refer to nebular morphology with the usual coding.

We infer that the nebular expansion is related to the carbonaceous dust sequence, linking nebular evolution and dust evolution in particular for round and elliptical PNe. The scatter represents the PN spread in progenitor mass and metallicity.

4. Discussion

In our analysis we found that 56% of the Magellanic Cloud PNe studied present solid state features, superimposed on the thermal dust continuum. These solid state features are, in 87% of cases, the signature of carbonaceous dust, with only a few PNe showing oxygen-rich dust emission instead. The rest of the nebulae show only nebular emission lines on a thermal continuum, in some cases very low. By contrast, such a low continuum and absence of features has not been observed in Galactic PNe (García-Lario et al., in preparation). It is remarkable that in the low-metallicity environments of the Magellanic Clouds the solid state features seem to be rarer than in Galactic PNe. This simple observation shows that the metallicity of the population has an enormous impact on the dust that forms on the AGB, as we knew already from carbon star counts in the Local Group Galaxies. What is new here is that the nature of the dust in PNe is different for different environments. Mass-loss, if caused by pressure on the dust grains, must vary accordingly. The selection effects are different for Galactic and Magellanic Cloud PNe, and a quantitative comparison of the Magellanic Cloud and Galactic samples is beyond the scope of this paper, but it is important to note that the selection effects that affect the LMC and SMC samples are comparable, thus the two samples readily comparable.

The ratio of CRD versus ORD PNe is 11 in the SMC, and 4.5 in the LMC, compared to ~ 1 in the Galaxy (García-Lario et al., in preparation). Selection effects limit the quantitative impact of the comparison between Magellanic Cloud PNe and the Galactic results. The evolution of carbonaceous dust proceeds from the amorphous state, to crystalline, to PAH; the grains evolve from small clusters of molecules to ionized PAH, as the central star becomes hotter (Peeters et al. 2004; Moutou et al. 2000). The grains become bigger but eventually evaporate under the action of the UV radiation field; thus, at late evolutionary stages we would not observe much dust in PNe. Not only is the dust chemistry different in different environments, but the evolutionary stage of the dust grains is also statistically different. For example, the SiC compounds are found only in SMC PNe and not in the LMC (or their Galactic) counterparts. In our sample there are three SMC PNe (SMP SMC 15, SMP SMC 18, and SMP SMC 20) with broad SiC emission, but none in the LMC. Given that the LMC sample is larger than the SMC sample, this is remarkable and of course needs to be studied with larger samples in both galaxies. A few other SMC and LMC

PNe have broad carbonaceous dust emission, such as SMP SMC 13, SMP LMC 25, and SMP LMC 48. Overall, features of amorphous dust grains are more common in the SMC than in the LMC PNe and are very uncommon in the Galaxy. If these structures really are the early evolutionary stages of PAHs, then we have found that the PN evolutionary rate depends strongly on population metallicity.

We found that there are strong correlations between the dust type, the carbon abundance, and the IR integrated luminosity. CRD and ORD PNe are generally IR-bright, and at the opposite extremes of the carbon abundance range. All CRD PNe have $C/O > 1$, and all ORD PNe have $C/O < 1$. Most of the F PNe are low IR-luminous objects, suggesting that some of them might be an evolved version of the other type of PNe. All CRD PNe are either round or elliptical in shape, some with a bipolar core, but none of them show extended lobes or other marked asymmetries. The opposite is true for ORD PNe.

The dust temperature correlates well with other physical parameters that change with evolution, (e.g., the nebular radius, the IR-luminosity, and the electron density). CRD PNe define a tight sequence on the $\log T_d$ – $\log R$ plane (where R is the photometric radii of the PNe) similar to those found in Galactic PNe. The CRD PNe whose spectra shows amorphous carbonaceous dust grains, such as SiC, have small physical radii, high electron density, and high IR-luminosity, in agreement with their being the unevolved version of PNe with PAH emission. Our empirical evolutionary sequence of carbonaceous dust features correlates well with the physical dimension of the nebulae, and their dust temperatures. Other correlations of IRS spectral type with excitation classes, and a modeling approach to these data will be thoroughly discussed in a future paper (Stanghellini et al., in preparation).

We have placed the central stars of the nebulae studied on the HR diagram and compared the central star locus with the evolutionary tracks for these post-AGB stars. We find strong systematics relating the dust type and the loci of their central stars on the HR diagram. For example, most F PNe are hosted by evolved central stars, their dust features having probably disappeared due to the UV radiation field of their central stars. We also find that central stars of CRD PNe are spread through the diagram, with the uncertain classified at low luminosity, and the only SiC PNe for which we have the HR locus is in the early evolutionary stage for the central star as well. The last row of Table 4 clearly hints that CRD PNe have central stars that are typical for the galaxy they belong to (see Villaver et al. 2006), while the only ORD PNe with measured mass is very massive. We need several more data points to substantiate this finding.

Our observations show that there are fundamental differences in the characteristics of the grains formed around PNe at different metallicities, which are a consequence of the more inefficient production of dust, the smaller mass-loss rates and slower evolution of the central

star experienced by PNe at low metallicities compared to their Galactic analogs. At the low metallicities of the Magellanic Clouds fewer grains are formed, with respect to their Galactic counterparts. The dust features that we see in our targets are of moderate strengths.

5. Conclusions

The IRS spectra of a selection of Large and Small Magellanic Cloud PNe were analyzed for their dust content to determine the nature of their dust chemistry and to gain knowledge of their dust evolutionary phase. The spectra studied show three major dust emission profiles, and we classify them into: F, those dominated by nebular emission lines; CRD, whose spectra show carbonaceous dust; and ORD, with oxygen-rich dust compounds seen in emission.

The dust properties, including dust type, IR luminosity, and dust temperatures, do correlate strongly with the known gas properties of the PNe. We find an exclusive correlation between dust type and carbon abundance, showing that *all CRD PNe have $C/O > 1$, and all ORD PNe have gone through the HBB phase*. We also find an exclusive correlation between CRD PNe and symmetric morphology, while all ORD PNe show high asymmetries. We also find hints of more massive central stars in ORD PNe.

The dust temperature decreases with increasing physical radii, and with decreasing electron density. CRD PNe define a scattered evolutionary sequence, the scatter being due to the range of initial masses and metallicity within the sample.

The statistics of dust emission features that we see in the Magellanic Clouds, if compared with that of the Galaxy, indicate that low metallicity environments do not favor the production of dust. As a consequence, the mass loss must be lower if the mass ejection is due to pressure on the dust grains. In particular, the spectacular bipolar nebulae, if indeed more massive and evolved from massive progenitors, are rarer in the Magellanic Clouds than in the galaxy, and the findings of the dust properties of this work conform to this scenario.

The PN sample analyzed in this paper represents an important fraction of all the LMC and SMC PNe ever observed with *HST*. Further *HST* and Spitzer observations on a larger Magellanic Cloud PN sample, such as shown in the outer contours of Figure 1, would be a good complement to this study. While the present Spitzer capabilities limit spectroscopic studies to bright Magellanic Cloud PNe, future space technology might extend the analysis to VLE PNe, such as those found in recent surveys (Reid & Parker 2006ab).

A comparative study of the LMC and SMC PNe together with those in the Galaxy, based on their mid-IR spectra, is also planned for the future.

Support for this work was provided by NASA through a grant issued by JPL/Caltech. Arturo Manchado, Letizia Stanghellini, and Eva Villaver are grateful to the European Space Astronomy Centre for their hospitality during two science group meetings. Arturo Manchado acknowledges support from grant *AYA 2004–3136* from the Spanish Ministerio de Educación y Ciencia. We warmly thank Terry Mahoney for carefully reading the manuscript. We acknowledge the input from an anonymous referee.

REFERENCES

- Caputo, F., Marconi, M., & Ripepi, V. 1999, *ApJ*, 525, 784
- Cioni, M.-R. L., et al. 2003, *A&A*, 406, 51
- Cioni, M.-R. L., & Habing, H. J. 2003, *A&A*, 402, 133
- Cohen, M., & Barlow, M. J. 1974, *ApJ*, 193, 401
- Freedman, W. L., et al. 2001, *ApJ*, 553, 47
- Groenewegen, M. A. T., Blommaert, J. A. D. L., Cioni, M.-R., Okumura, K., Habing, H. J., Trams, N. R., & van Loon, J. T. 2000, *Memorie della Societa Astronomica Italiana*, 71, 639
- García-Hernández, D. A., García-Lario, P., Plez, B., Manchado, A., D’Antona, F., Lub, J., & Habing, H. 2007, *A&A*, 462, 711
- García-Lario, P., & Perea Calderón, J. V. 2003, *ESA SP-511: Exploiting the ISO Data Archive. Infrared Astronomy in the Internet Age*, 97
- Houck, J. R., et al. 2004, *ApJS*, 154, 18
- Jacoby, G. H., & De Marco, O. 2002, *AJ*, 123, 269
- Kaeuff, H. U., Renzini, A., & Stanghellini, L. 1993, *ApJ*, 410, 251
- Leisy, P., & Dennefeld, M. 1996, *A&AS*, 116, 95
- Lenzuni, P., Natta, A., & Panagia, N. 1989, *ApJ*, 345, 306
- Marigo, P. 2001, *A&A*, 370, 194
- Mould, J. R., et al. 2000, *ApJ*, 529, 786

- Moutou, C., Verstraete, L., Léger, A., Sellgren, K., & Schmidt, W. 2000, *A&A*, 354, L17
- Peeters, E., Mattioda, A. L., Hudgins, D. M., & Allamandola, L. J. 2004, *ApJ*, 617, L65
- Peimbert, M., & Serrano, A. 1980, *Revista Mexicana de Astronomia y Astrofisica*, 5, 9
- Reid, W. A., & Parker, Q. A. 2006, *MNRAS*, 373, 521
- Reid, W. A., & Parker, Q. A. 2006, *MNRAS*, 365, 401
- Shaw, R. A., Stanghellini, L., Mutchler, M., Balick, B., & Blades, J. C. 2001, *ApJ*, 548, 727
- Shaw, R. A., Stanghellini, L., Villaver, E., & Mutchler, M. 2006, *ApJS*, 167, 201
- Schultheis, M., Glass, I. S., & Cioni, M.-R. 2004, *A&A*, 427, 945
- Stanghellini, L., Blades, J. C., Osmer, S. J., Barlow, M. J., & Liu, X.-W. 1999, *ApJ*, 510, 687
- Stanghellini, L., & Renzini, A. 2000, *ApJ*, 542, 308
- Stanghellini, L., Shaw, R. A., Mutchler, M., Palen, S., Balick, B., & Blades, J. C. 2002, *ApJ*, 575, 178
- Stanghellini, L., Shaw, R. A., Balick, B., Mutchler, M., Blades, J. C., & Villaver, E. 2003, *ApJ*, 596, 997
- Stanghellini, L., Shaw, R. A., & Gilmore, D. 2005, *ApJ*, 622, 294
- Stanghellini, L. 2006, *ArXiv Astrophysics e-prints*, arXiv:astro-ph/0610206
- Trams, N. R., et al. 1999, *A&A*, 346, 843
- Vassiliadis, E., & Wood, P. R. 1993, *ApJ*, 413, 641
- Villaver, E., Manchado, A., & García-Segura, G. 2002, *ApJ*, 581, 1204
- Villaver, E., Stanghellini, L., & Shaw, R. A. 2007, *ApJ*, 656, 831
- Villaver, E., Stanghellini, L., & Shaw, R. A. 2004, *ApJ*, 614, 716
- Villaver, E., Stanghellini, L., & Shaw, R. A. 2003, *ApJ*, 597, 298
- Volk, K. 2003, *IAU Symposium*, 209, 281
- Werner, M., et al. 2004, *ApJS*, 154, 1

Westerlund, B. E. 1997, Book

Willson, L. A. 2000, ARA&A, 38, 573

Zhang, C. Y., & Kwok, S. 1991, A&A, 250, 179

Table 1. Target Selection

Object	R ["]	Morphology	notes
SMP LMC 4	0.69	Elliptical	Faint halo
SMP LMC 9	0.46	Bipolar core	Barrel shape
SMP LMC 10	0.88	Pointsymmetric	Spiral shape
SMP LMC 16	1.00	Bipolar	
SMP LMC 18	0.51	Round	Possibly Bipolare core
SMP LMC 19	0.41	Bipolar core	Ring
SMP LMC 20	0.41	Bipolar core	
SMP LMC 21	0.58	Quadrupolar	
SMP LMC 25	0.23	Round	
SMP LMC 27	0.46	Quadrupolar	Outer arc and halo
SMP LMC 34	0.32	Elliptical	
SMP LMC 45	0.72	Bipolar	Questionable morphology
SMP LMC 46	0.31	Bipolar core	Possible ring
SMP LMC 48	0.20	Elliptical	
SMP LMC 66	0.54	Elliptical	
SMP LMC 71	0.31	Elliptical	
SMP LMC 72	...	Bipolar	
SMP LMC 79	0.22	Bipolar core	
SMP LMC 80	0.21	Round	
SMP LMC 81	0.15	Round	Barely resolved
SMP LMC 95	0.46	Bipolar core	Ansa
SMP LMC 97	0.59	Round	
SMP LMC 99	0.41	Bipolar core	
SMP LMC 100	0.71	Bipolar core	Possibly quadrupolar
SMP LMC 102	0.71	Round	Possibly Bipolar core
SMP SMC 2	0.25	Round	
SMP SMC 5	0.31	Round	
SMP SMC 8	0.23	Round	
SMP SMC 9	0.55	Round	Inner structure

Table 1—Continued

Object	R ["]	Morphology	notes
SMP SMC 13	0.19	Round	
SMP SMC 14	0.42	Round	Ansaes and/or inner structure
SMP SMC 15	0.17	Round	
SMP SMC 16	0.18	Elliptical	
SMP SMC 17	0.25	Elliptical	Faint detached halo
SMP SMC 18	0.15	...	Unresolved
SMP SMC 19	0.30	Round	Outer structure
SMP SMC 20	0.15	...	Unresolved
SMP SMC 23	0.30	Bipolar core	
SMP SMC 25	0.19	Elliptical	
SMP SMC 26	0.28	Pointsymmetric	
SMP SMC 27	0.23	Round	Attached outer halo

Table 2. Observing log

Object	R.A. J2000.0	DEC J2000.0	Obs. date	ID number	IRS campaign
SMP LMC 4	04 ^h 43 ^m 21 ^s .50	−71°30′09″.5	08/14/2005	14703360	23.2
SMP LMC 9	04 ^h 50 ^m 24 ^s .71	−68°13′17″.0	09/13/2005	14705920	24
SMP LMC 10	04 ^h 51 ^m 08 ^s .90	−68°49′05″.8	09/13/2005	14700032	24
SMP LMC 16	05 ^h 02 ^m 01 ^s .91	−69°48′54″.4	08/14/2005	14700288	23.2
SMP LMC 18	05 ^h 03 ^m 42 ^s .64	−70°06′47″.8	08/14/2005	14700544	23.2
SMP LMC 19	05 ^h 03 ^m 41 ^s .30	−70°13′53″.6	08/14/2005	14700800	23.2
SMP LMC 20	05 ^h 04 ^m 40 ^s .14	−69°21′39″.3	08/14/2005	14701056	23.2
SMP LMC 21	05 ^h 04 ^m 51 ^s .90	−68°39′10″.0	08/14/2005	14701312	23.2
SMP LMC 25	05 ^h 06 ^m 24 ^s .00	−69°03′19″.2	08/14/2005	14701568	23.2
SMP LMC 27	05 ^h 07 ^m 54 ^s .90	−66°57′46″.1	09/13/2005	14701824	24
SMP LMC 34	05 ^h 10 ^m 17 ^s .18	−68°48′23″.0	08/14/2005	14702336	23.2
SMP LMC 45	05 ^h 19 ^m 21 ^s .00	−66°58′13″.0	07/14/2005	14702592	22
SMP LMC 46	05 ^h 19 ^m 29 ^s .72	−68°51′09″.1	08/11/2005	14702848	23.2
SMP LMC 48	05 ^h 20 ^m 09 ^s .66	−69°53′39″.2	08/14/2005	14703104	23.2
SMP LMC 66	05 ^h 28 ^m 41 ^s .20	−67°33′39″.0	08/11/2005	14703616	23.2
SMP LMC 71	05 ^h 30 ^m 33 ^s .22	−70°44′38″.4	08/11/2005	14703872	23.2
SMP LMC 72	05 ^h 30 ^m 45 ^s .98	−70°50′16″.4	08/11/2005	14704128	23.2
SMP LMC 79	05 ^h 34 ^m 08 ^s .76	−74°20′06″.6	10/10/2005	14704384	25
SMP LMC 80	05 ^h 34 ^m 38 ^s .87	−70°19′56″.9	08/11/2005	14704640	23.2
SMP LMC 81	05 ^h 35 ^m 20 ^s .92	−73°55′30″.1	10/10/2005	14704896	25
SMP LMC 95	06 ^h 01 ^m 45 ^s .30	−67°56′08″.0	08/11/2005	14705152	23.2
SMP LMC 97	06 ^h 10 ^m 25 ^s .50	−67°56′21″.0	08/11/2005	14705408	23.2
SMP LMC 99	06 ^h 18 ^m 58 ^s .21	−71°35′50″.7	10/15/2005	14705664	25
SMP LMC 100	06 ^h 22 ^m 55 ^s .73	−72°07′41″.4	11/14/2005	14699520	26
SMP LMC 102	06 ^h 29 ^m 32 ^s .93	−68°03′32″.9	08/11/2005	14699776	23.2
SMP SMC 2	00 ^h 32 ^m 38 ^s .81	−71°41′58″.7	08/14/2005	14709248	23.2
SMP SMC 5	00 ^h 41 ^m 21 ^s .67	−72°45′18″.0	08/14/2005	14709504	23.2
SMP SMC 8	00 ^h 43 ^m 25 ^s .17	−72°38′18″.9	08/14/2005	14709760	23.2

Table 2—Continued

Object	R.A. J2000.0	DEC J2000.0	Obs. date	ID number	IRS campaign
SMP SMC 9	00 ^h 45 ^m 20 ^s .66	−73°24′10″.5	08/14/2005	14710016	23.2
SMP SMC 13	00 ^h 49 ^m 51 ^s .71	−73°44′21″.3	08/14/2005	14706176	23.2
SMP SMC 14	00 ^h 50 ^m 34 ^s .99	−73°42′57″.9	08/14/2005	14706432	23.2
SMP SMC 15	00 ^h 51 ^m 07 ^s .45	−73°57′37″.1	08/14/2005	14706688	23.2
SMP SMC 16	00 ^h 51 ^m 27 ^s .08	−72°26′11″.1	08/14/2005	14706944	23.2
SMP SMC 17	00 ^h 51 ^m 56 ^s .44	−71°24′44″.1	08/08/2005	14707200	23.2
SMP SMC 18	00 ^h 51 ^m 57 ^s .97	−73°20′30″.1	08/14/2005	14707456	23.2
SMP SMC 19	00 ^h 53 ^m 11 ^s .14	−72°45′07″.5	08/14/2005	14707712	23.2
SMP SMC 20	00 ^h 56 ^m 05 ^s .39	−70°19′24″.7	08/08/2005	14707968	23.2
SMP SMC 23	00 ^h 58 ^m 42 ^s .14	−72°56′59″.6	08/14/2005	14708224	23.2
SMP SMC 25	00 ^h 59 ^m 40 ^s .51	−71°38′15″.3	08/14/2005	14708480	23.2
SMP SMC 26	01 ^h 04 ^m 17 ^s .81	−73°21′51″.2	08/14/2005	14708736	23.2
SMP SMC 27	01 ^h 21 ^m 10 ^s .67	−73°14′35″.4	08/14/2005	14708992	23.2

Table 3. Characteristics of the IRS spectra

Object	T_{dust} [K]	$\log F_{\text{IR}}$ [erg cm ⁻² s ⁻¹]	IRE	Dust type	Excitation
SMP LMC 4	190	-11.7	2.65	F	very high
SMP LMC 9	140	-11.7	0.86	CRD	very high
SMP LMC 10	90	-12.5	0.10	F	high
SMP LMC 16	80	-12.3	0.39	F	very high
SMP LMC 18	110	-11.9	1.2	F	intermediate
SMP LMC 19	130	-11.3	1.05	CRD	very high
SMP LMC 20	90	-12.3	0.24	F	very high
SMP LMC 21	130	-11.1	20.96	ORD	very high
SMP LMC 25	160	-10.7	1.52	CRD	intermediate
SMP LMC 27	140	-11.9	1.75	F	intermediate
SMP LMC 34	130	-11.4	1.40	F	intermediate
SMP LMC 45	120	-11.9	0.30	F	high
SMP LMC 46	140	-11.9	1.37	CRD	high
SMP LMC 48	170	-10.8	1.43	CRD	intermediate
SMP LMC 66	140	-11.6	0.96	F	high
SMP LMC 71	150	-10.9	2.72	CRD	very high
SMP LMC 72	60	-13.0	1.88	F	very high
SMP LMC 79	170	-10.9	2.64	CRD	high
SMP LMC 80	110	-13.1	0.05	F	intermediate
SMP LMC 81	130	-10.6	2.79	ORD	intermediate
SMP LMC 95	110	-12.1	0.68	F	high
SMP LMC 97	130	-11.7	0.20	F	very high
SMP LMC 99	160	-11.0	0.68	CRD	very high
SMP LMC 100	120	-11.5	0.74	CRD	very high
SMP LMC 102	140	-12.1	0.62	F	high
SMP SMC 2	160	-11.5	0.79	CRD	very high
SMP SMC 5	180	-11.1	...	CRD	very high
SMP SMC 8	160	-11.7	0.49	F	intermediate

Table 3—Continued

Object	T_{dust} [K]	$\log F_{\text{IR}}$ [erg cm ⁻² s ⁻¹]	IRE	Dust type	Excitation
SMP SMC 9	120	-12.0	1.10	F	...
SMP SMC 13	190	-11.3	0.60	CRD	intermediate
SMP SMC 14	150	-11.6	0.91	CRD	high
SMP SMC 15	190	-10.8	2.03	CRD	intermediate
SMP SMC 16	180	-11.4	0.87	CRD	low
SMP SMC 17	160	-11.1	1.19	CRD	intermediate
SMP SMC 18	170	-10.8	2.37	CRD	intermediate
SMP SMC 19	150	-11.3	1.50	CRD	very high
SMP SMC 20	250	-11.0	1.22	CRD	intermediate
SMP SMC 23	150	-12.2	0.35	F	intermediate
SMP SMC 25	130	-11.5	1.86	ORD	very high
SMP SMC 26	130	-12.1	0.76	F	very high
SMP SMC 27	180	-11.4	0.47	CRD	intermediate

Table 4. Summary of relations

	LMC			SMC		
	F	CRD	ORD	F	CRD	ORD
Sample size	14	9	2	4	11	1
$\langle \text{C}/\text{H} \rangle \times 10^4$	(2.0 ± 2.0)	(4.3 ± 2.0)	(0.18 ± 0.05)	(4.2 ± 2.7)	(4.6 ± 2.0)	...
$\langle \text{N}/\text{H} \rangle \times 10^5$	(8.4 ± 0.1)	(7.6 ± 4.1)	(12 ± 15)	(7.4 ± 7.4)	(2.6 ± 1.7)	8.3
$\langle \text{O}/\text{H} \rangle \times 10^4$	(1.8 ± 1.0)	(2.4 ± 1.0)	(1.3 ± 0.7)	(2.1 ± 1.7)	(1.4 ± 0.6)	0.4
$\langle \text{Ne}/\text{H} \rangle \times 10^5$	(2.7 ± 1.5)	(4.1 ± 1.9)	(1.8 ± 0.4)	(3.4 ± 4.9)	(2.2 ± 1.6)	0.9
$\langle \text{M}/\text{M}_\odot \rangle$	(0.65 ± 0.13)	(0.63 ± 0.00)	...	0.59	(0.59 ± 0.05)	0.82

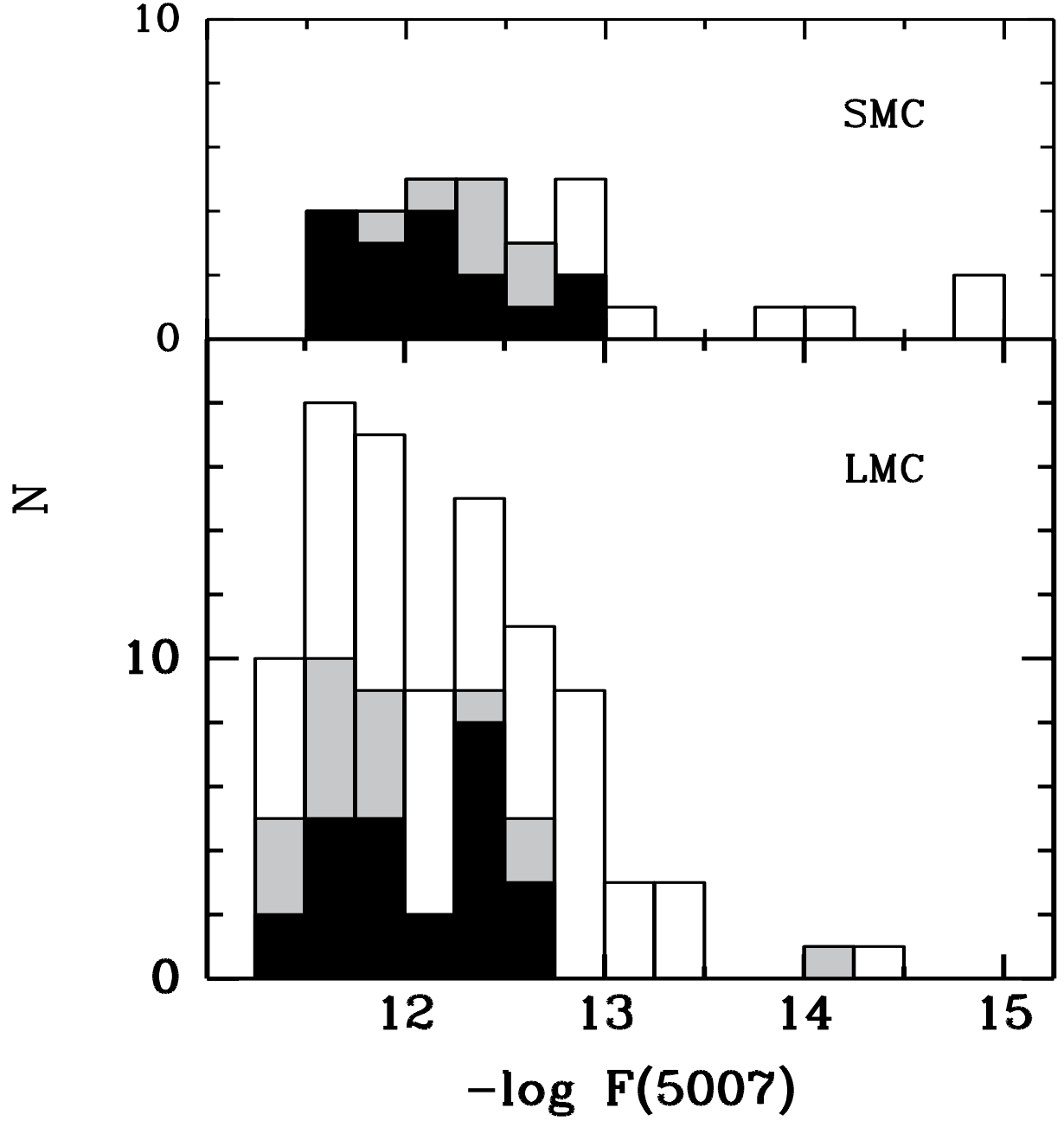


Fig. 1.— Histogram of the [O III] $\lambda 5007$ flux of Magellanic Cloud PNe whose size is smaller than $2''$ as measured on the *HST* images. Outer histogram: complete sample. Gray histogram: the ROC sample (i.e., the GTO program by Houck). Black histogram: the PN sample presented in this paper.

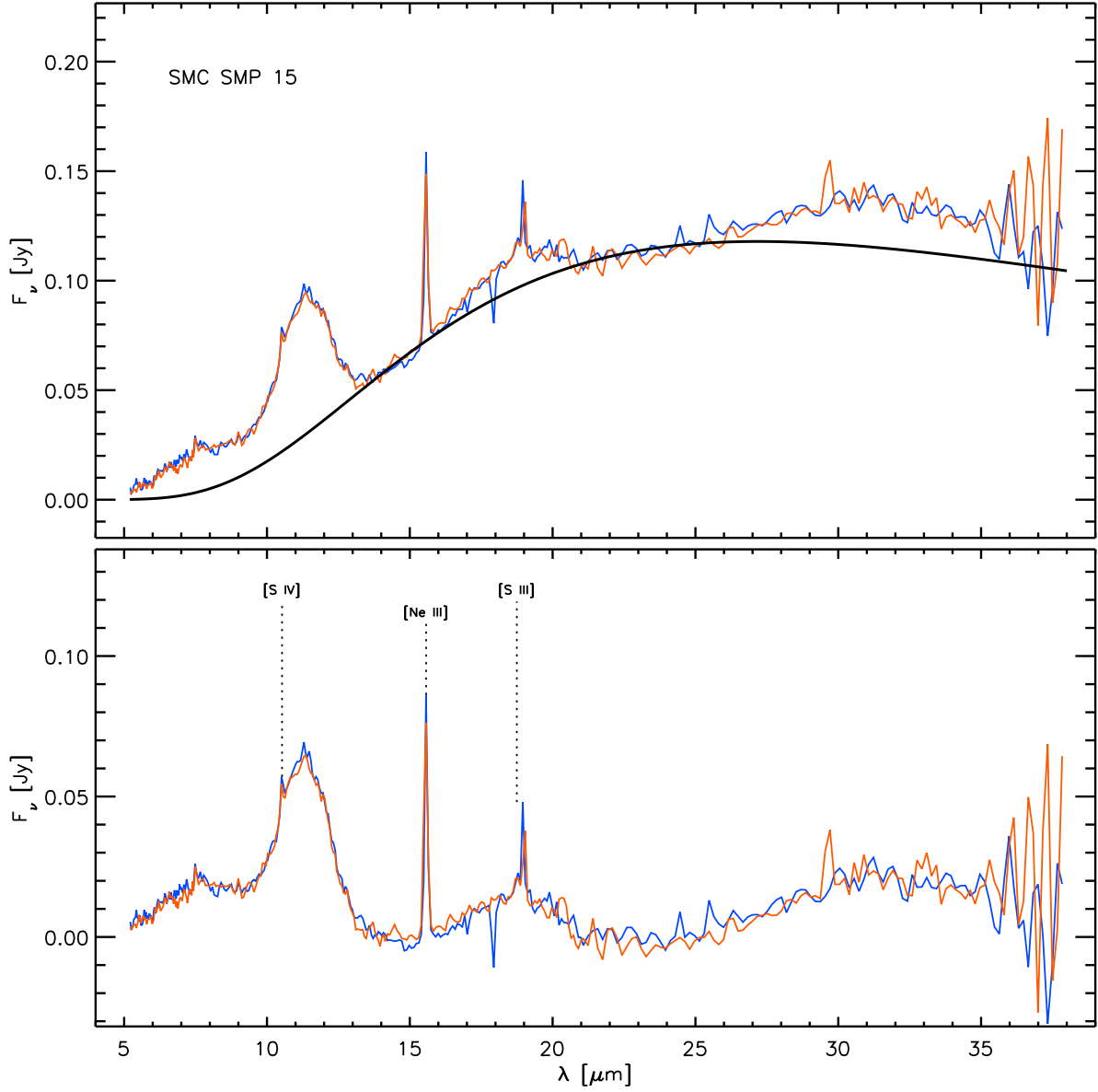


Fig. 2.— Continuum fitted (upper panel) and continuum-subtracted spectrum (lower panel) of SMP SMC 15. Both nod positions are shown, in thin lines. The thick line in the upper plot identifies the blackbody fit used. Note that the fit is correctly below the broad dust features: the large silicon carbide feature at $11\ \mu\text{m}$, the broad feature at $15\text{--}21\ \mu\text{m}$, and the broad feature peaking at $30\ \mu\text{m}$. Several nebular emission lines have been identified in the lower panel. The IRS spectral type of this PN is CRD (see text of §2.3 for spectral type definitions).

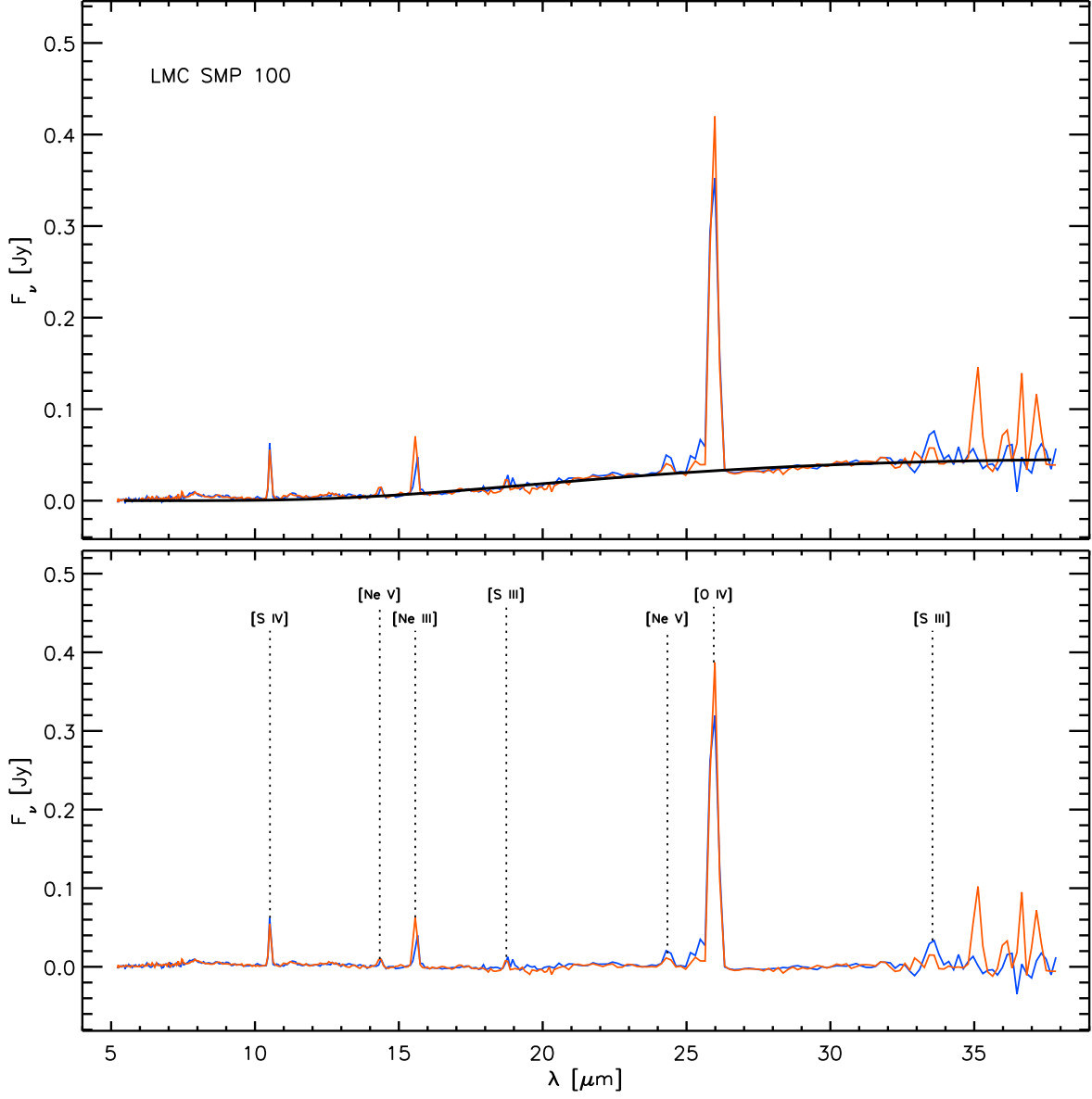


Fig. 3.— Same as in Fig. 2, for SMP LMC 100. The spectrum is dominated by the emission lines with only a faint carbonaceous dust features at 6.2 μm . The IRS spectral type of this PN is CRD.

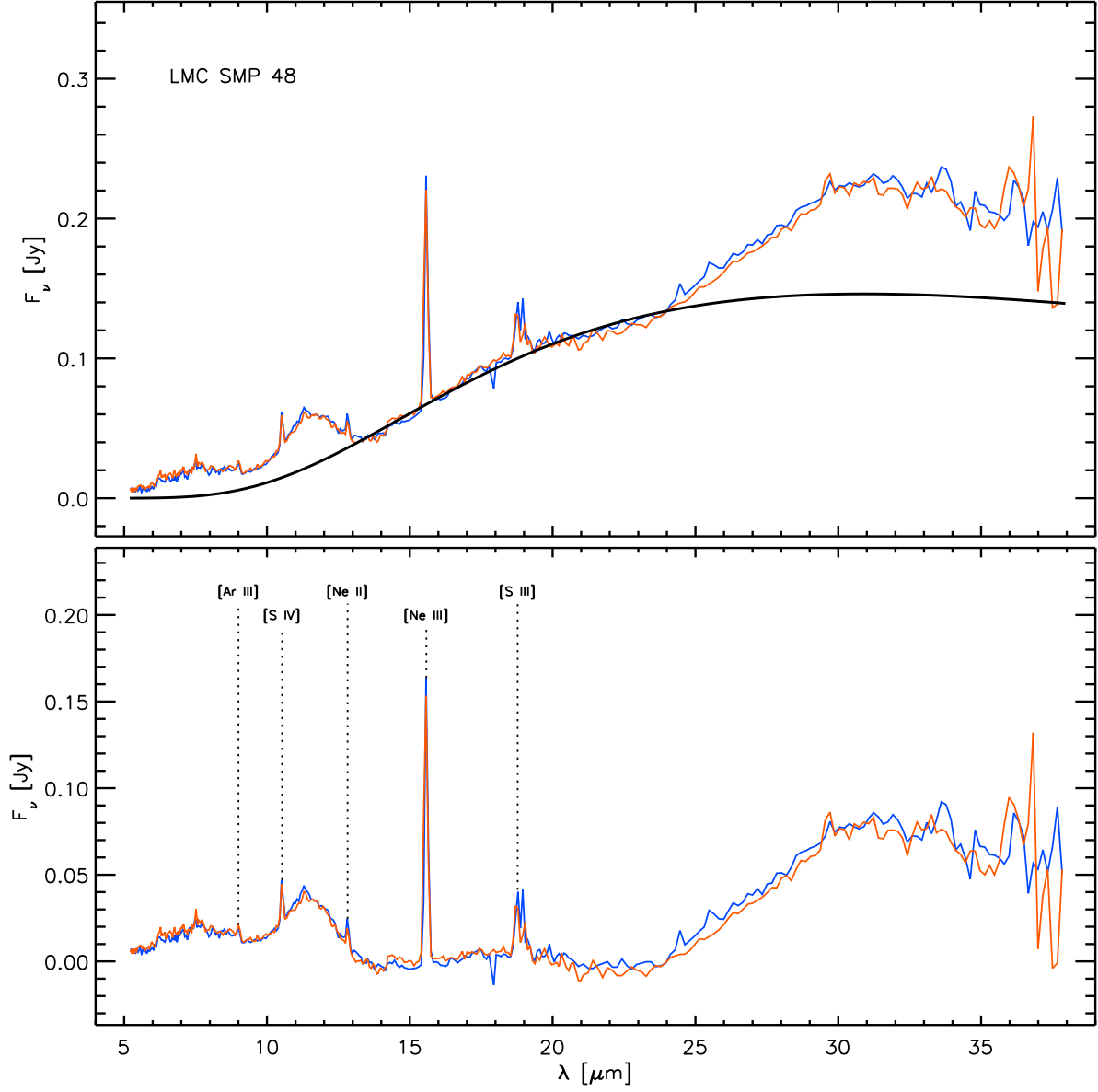


Fig. 4.— Same as in Fig. 2, for SMP LMC 48. The broad plateau feature at 6–9 μm and the remnant of a broad amorphous SiC feature at 11 μm are clearly detected in this spectrum, together with a very strong 30 μm feature. The IRS spectral type of this PN is CRD.

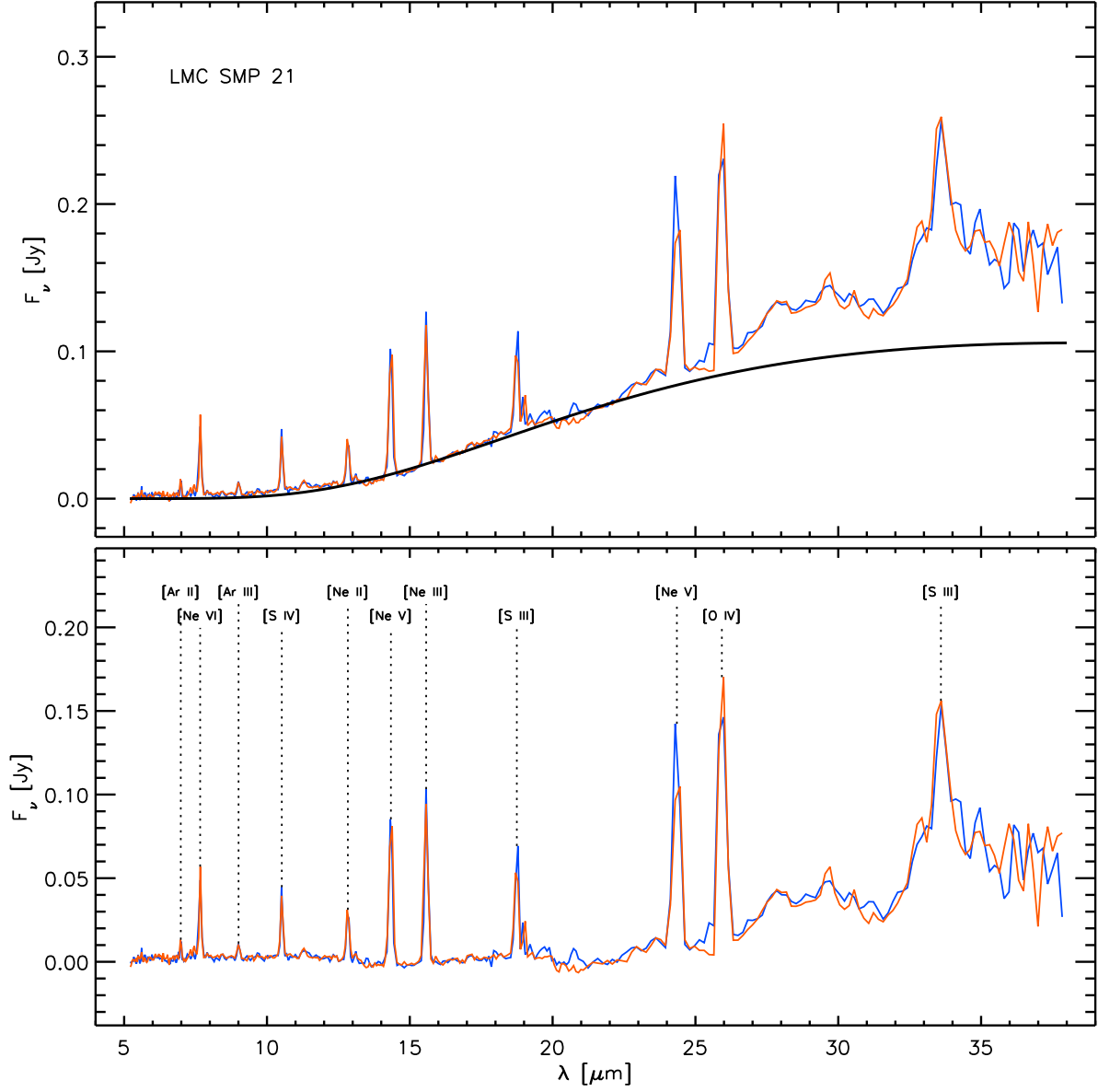


Fig. 5.— Same as in Fig. 2, for SMP LMC 21. The oxygen-rich dust features are seen at longer wavelengths. The IRS spectral type of this PN is ORD.

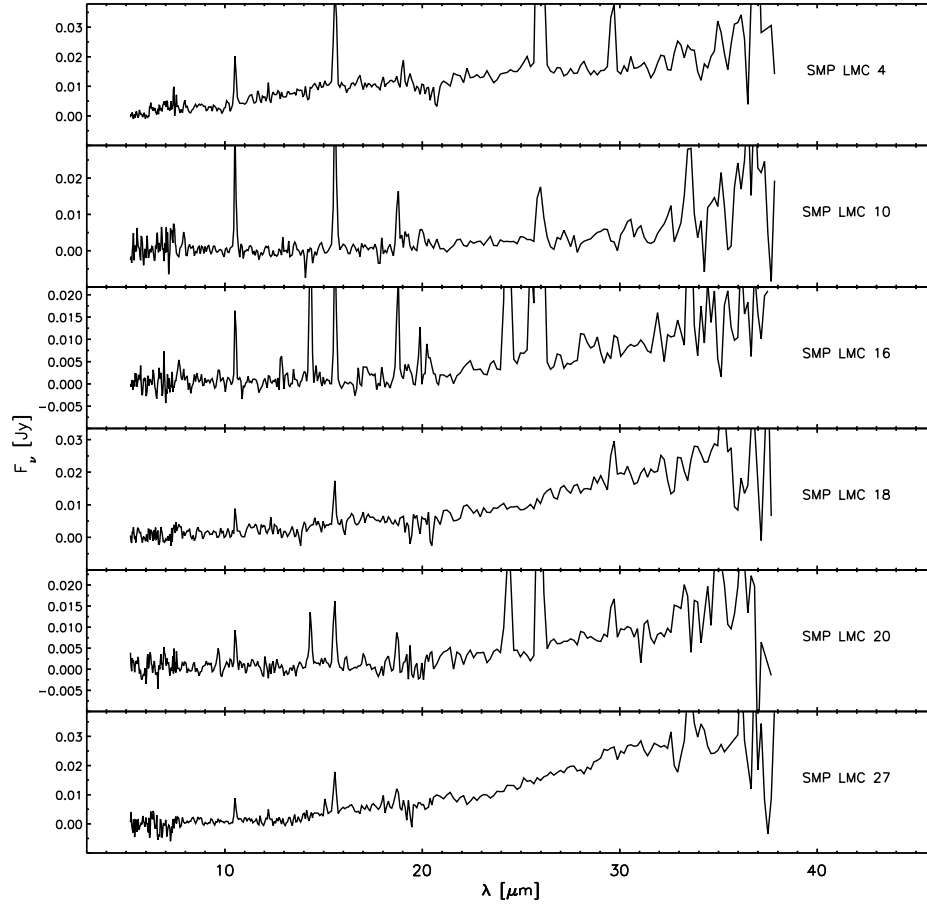


Fig. 6a.— IRS spectra of F PNe.

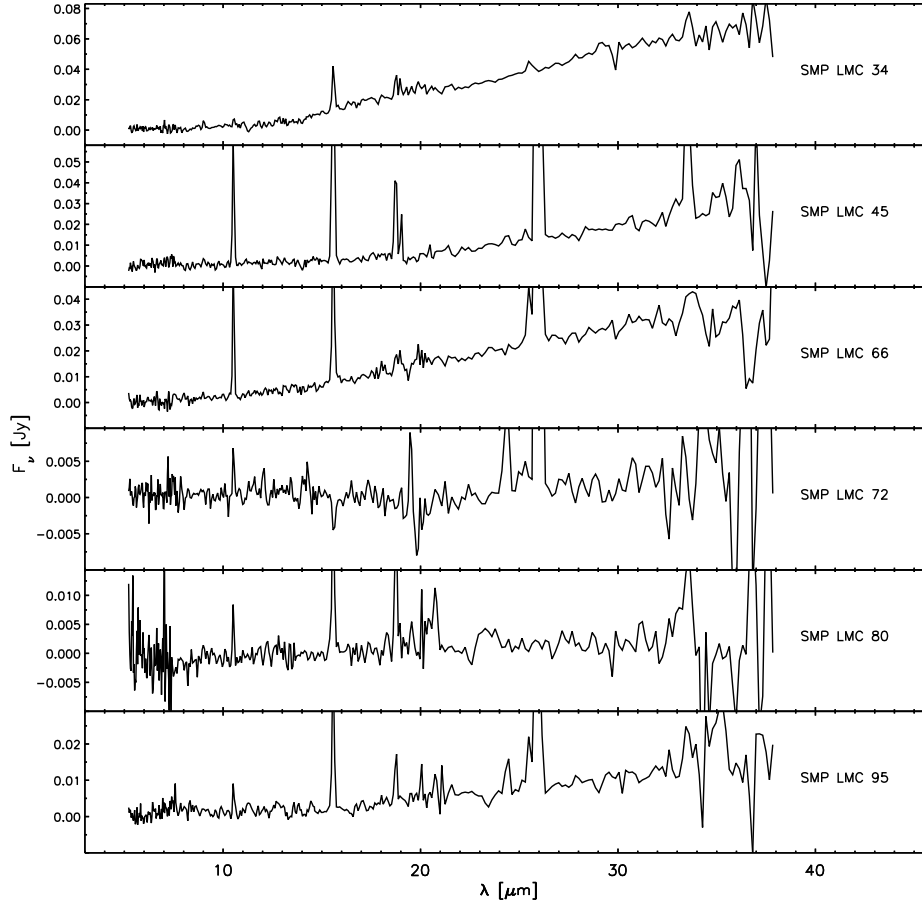


Fig. 6b. — Continued.

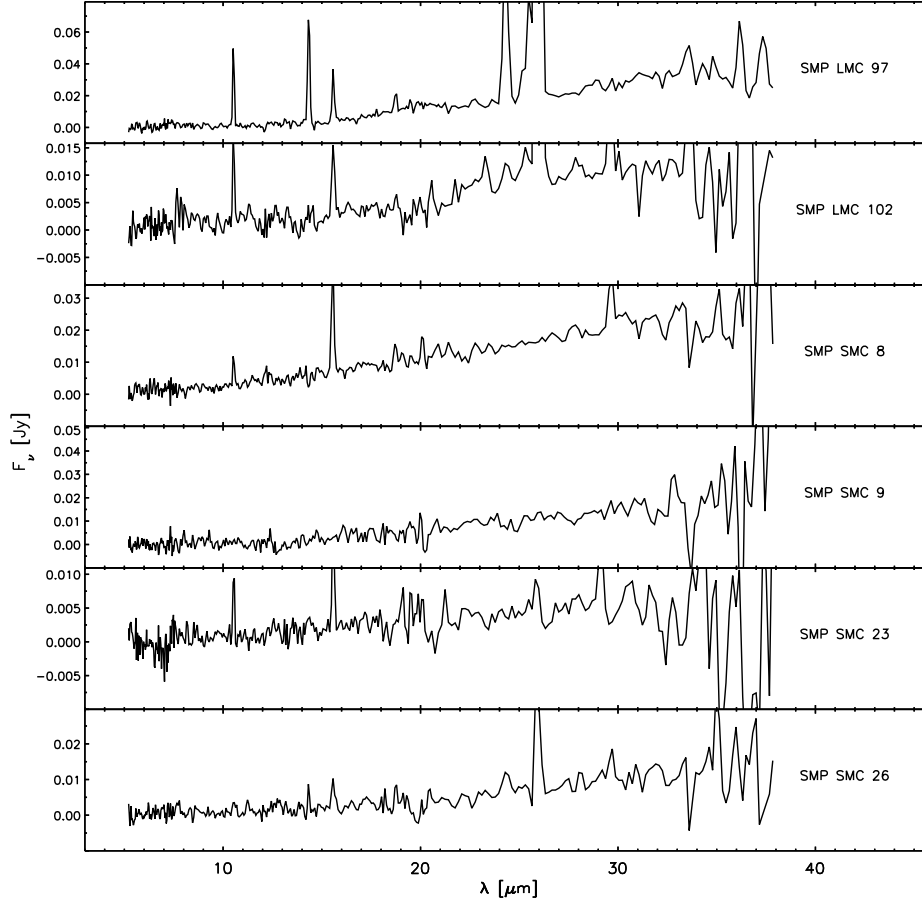


Fig. 6c. — Continued.

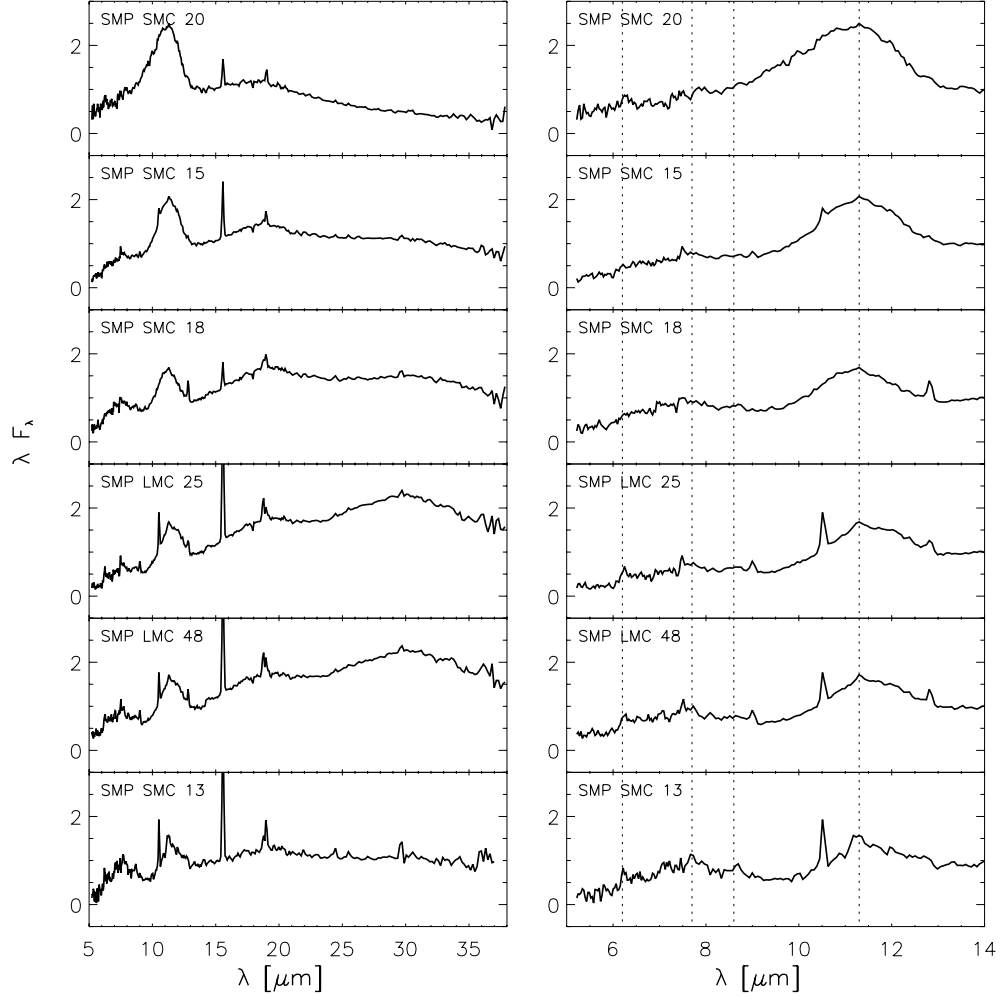


Fig. 7a.— IRS spectra of CRD PNe. Left panel: entire spectra. Right panels: the 5–14 μm spectra, where the vertical lines correspond to the classical PAH features at 6.2, 7.7, 8.6, and 11.3 μm .

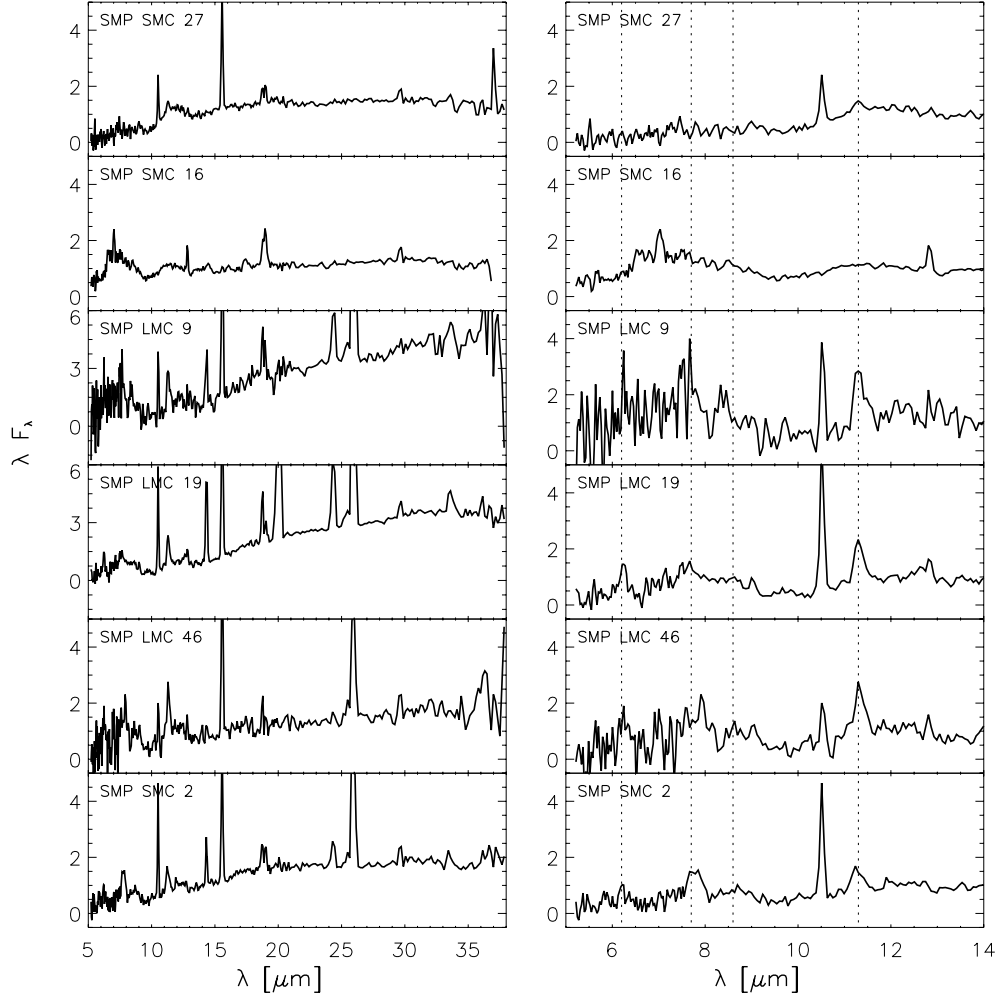


Fig. 7b. — Continued.

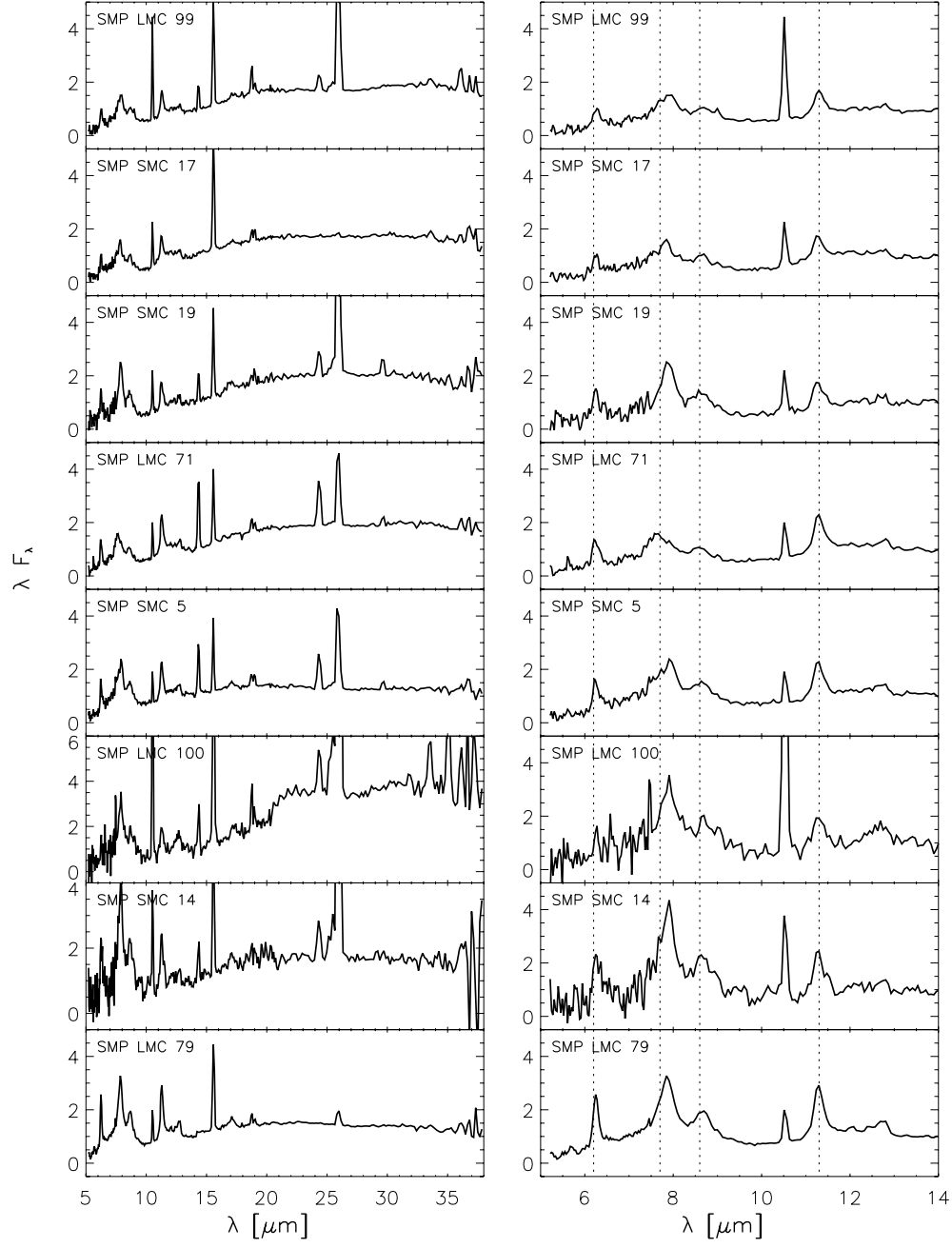


Fig. 7c. — Continued.

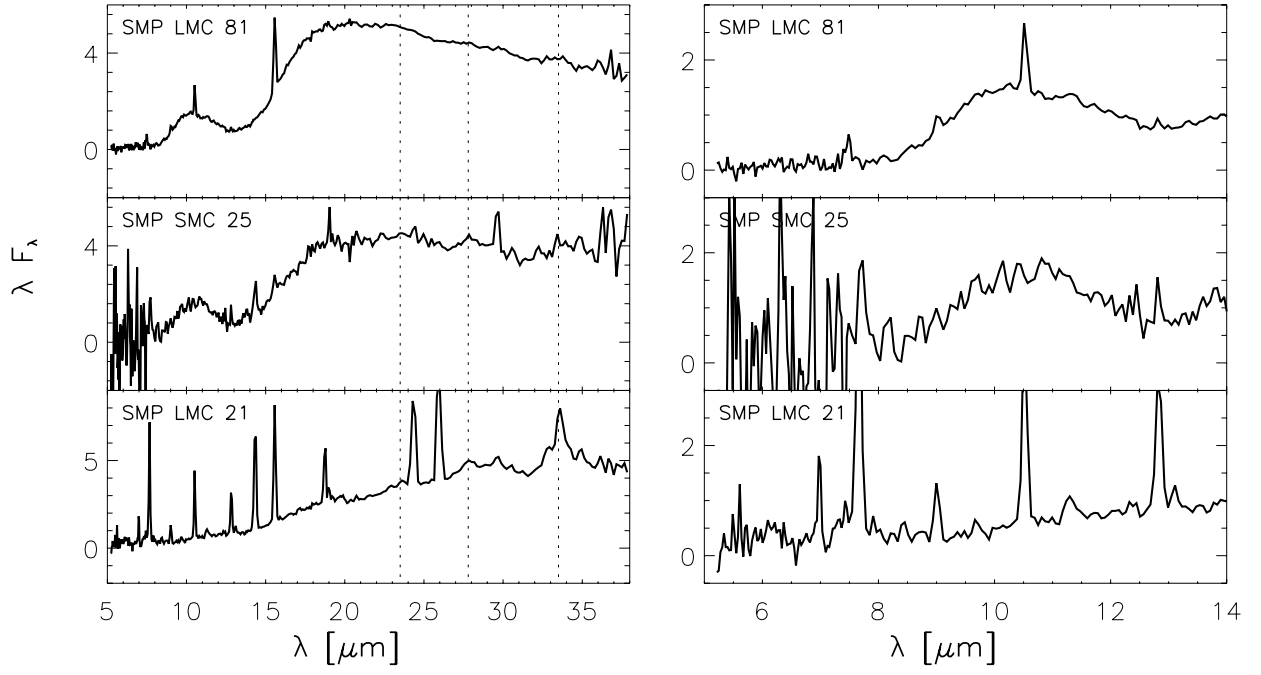


Fig. 8.— IRS spectra of ORD PNe. Left panel: entire spectra, where the vertical lines correspond to the crystalline silicate features at 23.5, 27.8, and 33.5 μm . Right panel: the 5–14 μm spectra.

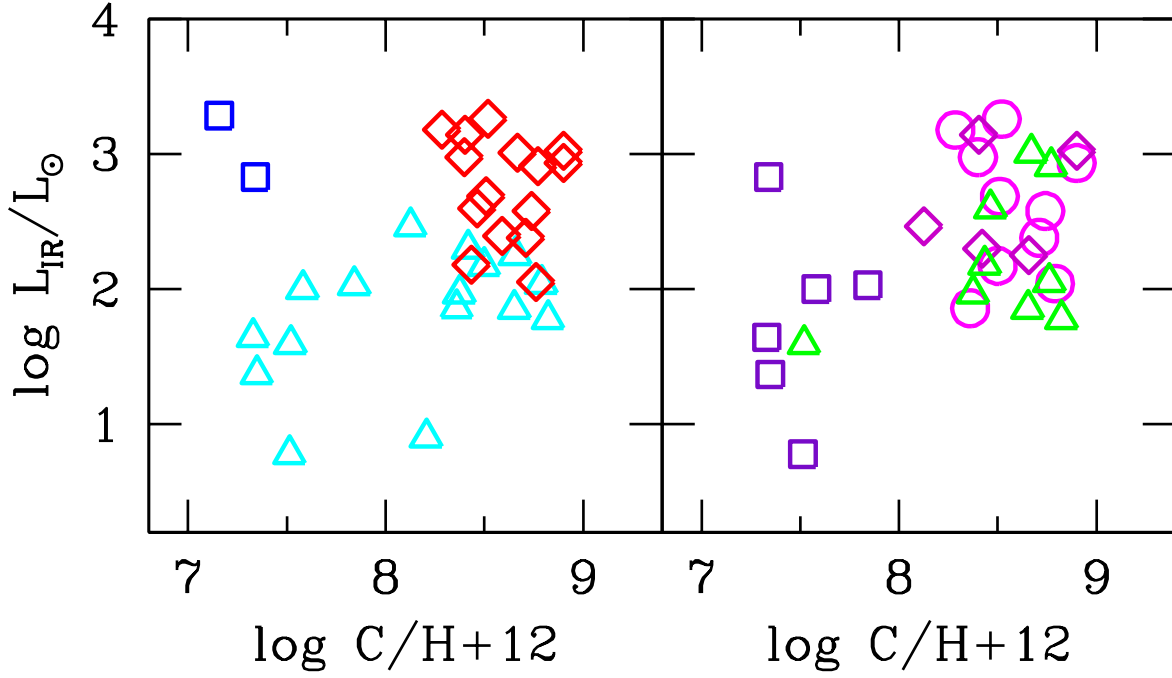


Fig. 9.— Infrared luminosity versus carbon abundance. Left panel: dust type is coded with triangles (F), diamonds (CRD), and squares (ORD). Right panel: morphology is coded with circles (Round), diamonds (Elliptical), triangles (Bipolar Core), and squares (Bipolar, Quadrupolar, and Pointsymmetric).

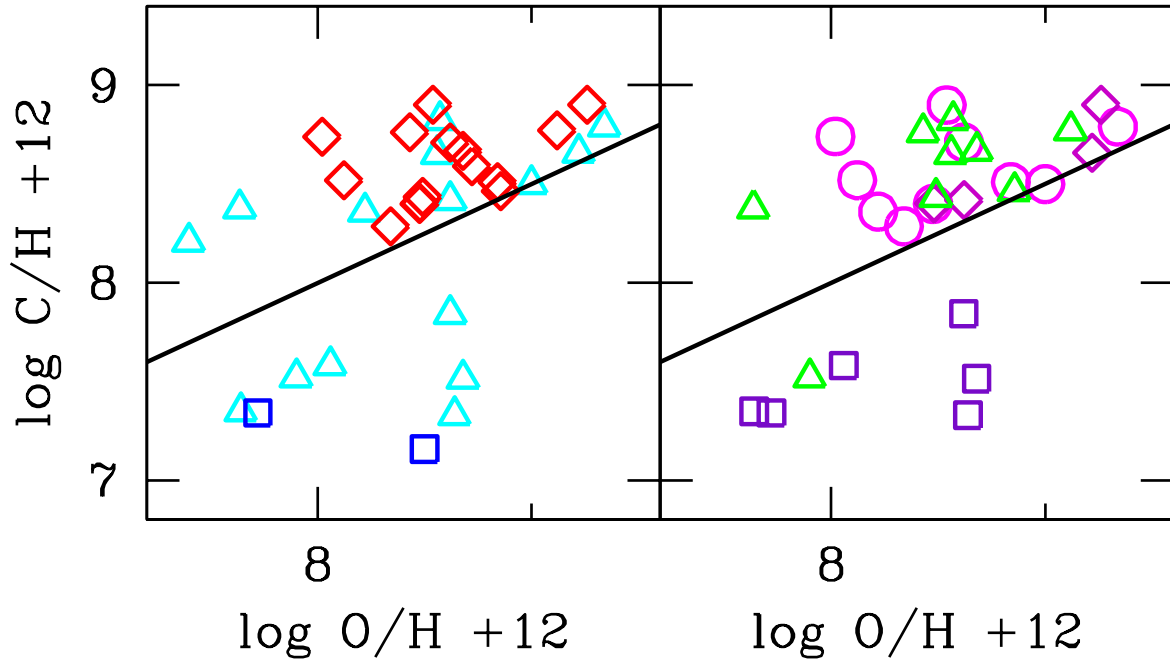


Fig. 10.— Carbon versus oxygen abundance of the gas of Magellanic Cloud PNe. Dust type (left panel) and morphology (right panel) are coded as in Fig. 9. The line represents $C/O=1$.

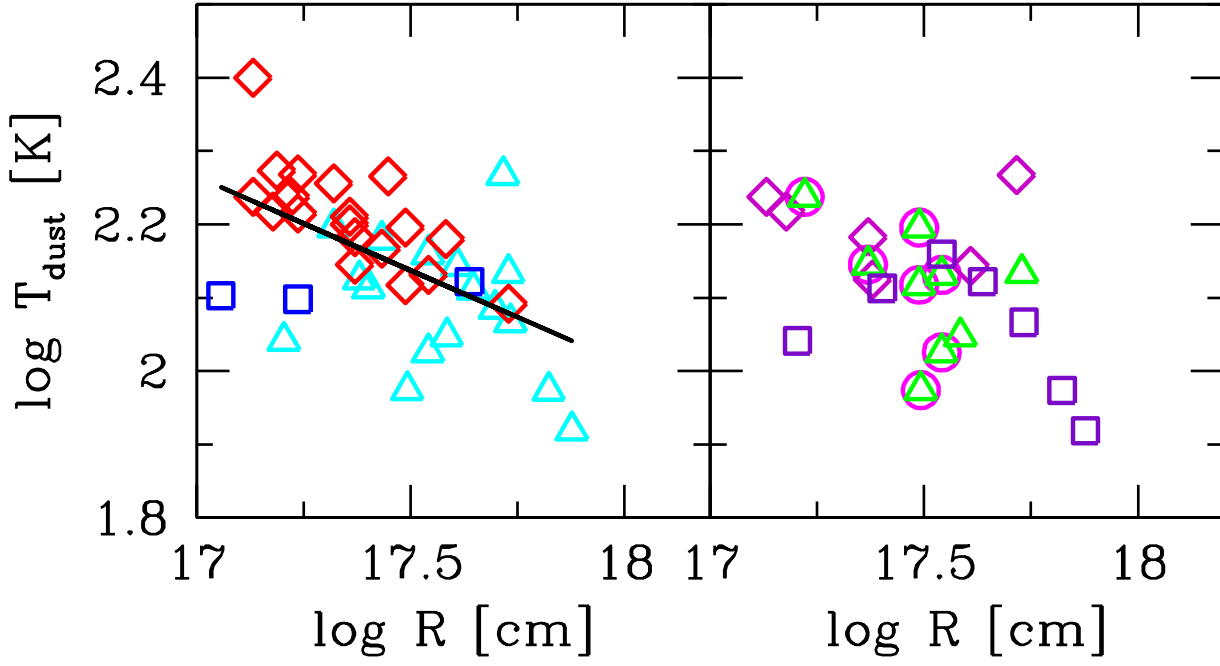


Fig. 11.— The relation between T_{dust} and physical radius. Symbols for dust type (left panel) and morphology (right panel) are coded as in Fig. 9. The line is the best fit to the data.

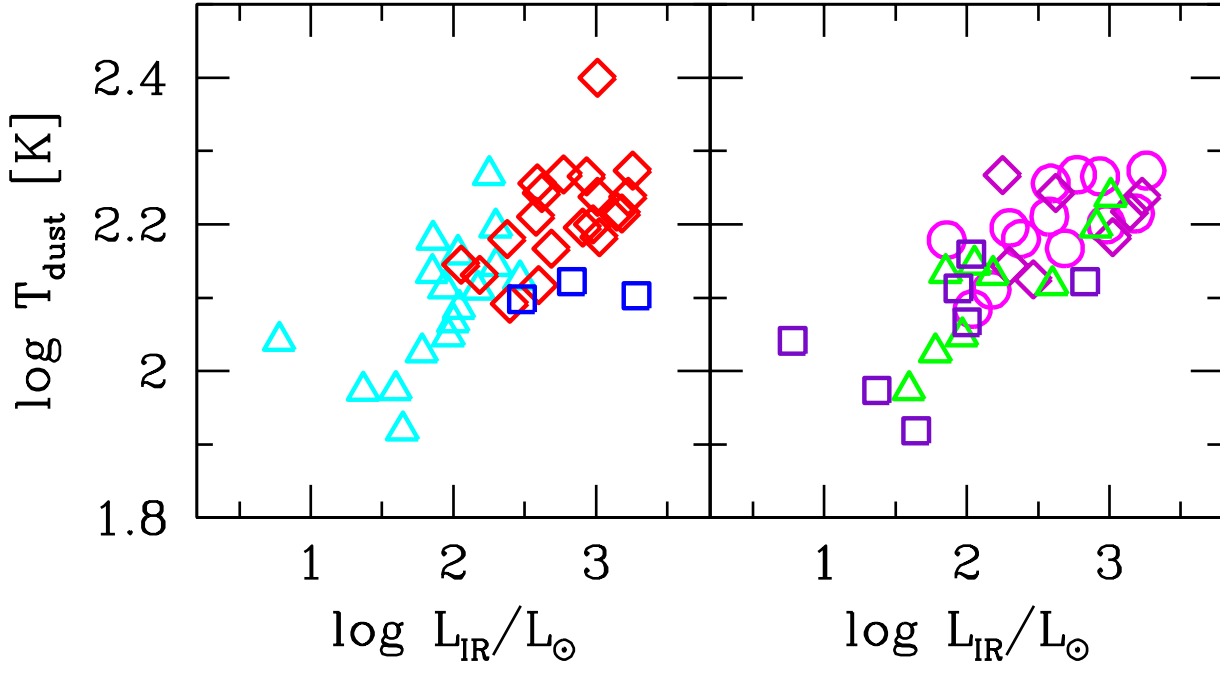


Fig. 12.— Dust temperature versus IR luminosity for dust type (left) and morphology (right). Symbols as in Fig. 9.

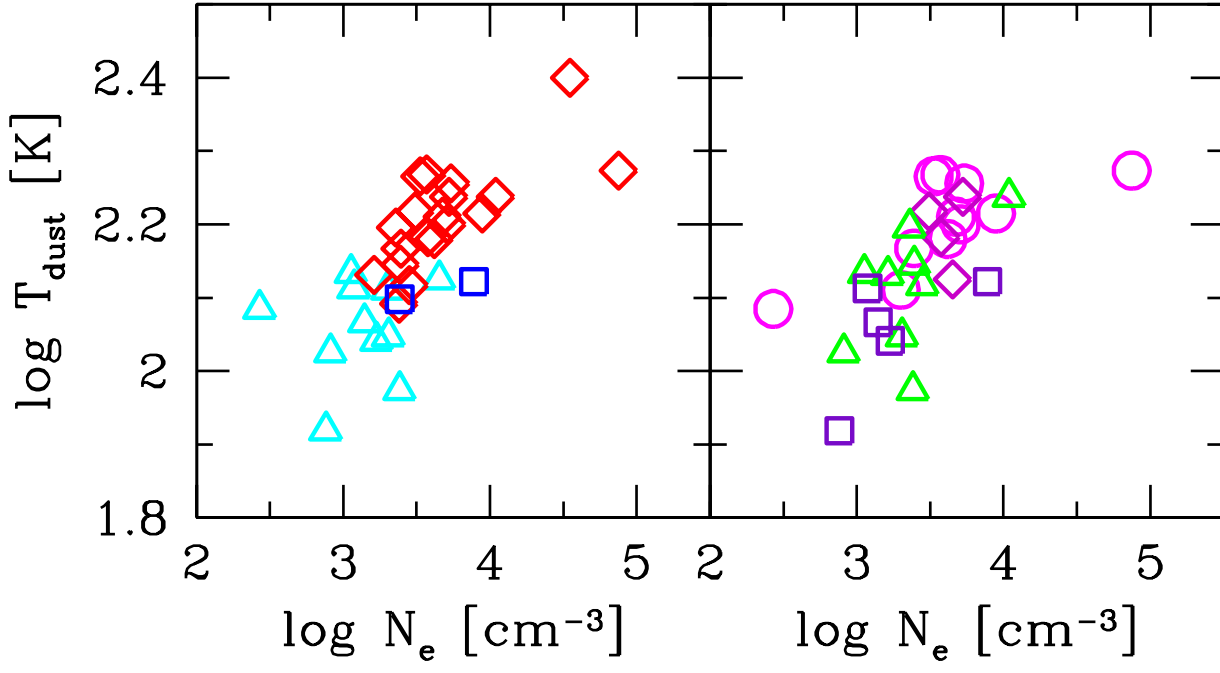


Fig. 13.— Dust temperature versus electron density for dust type (left) and morphology (right). Symbols as in Fig. 9.

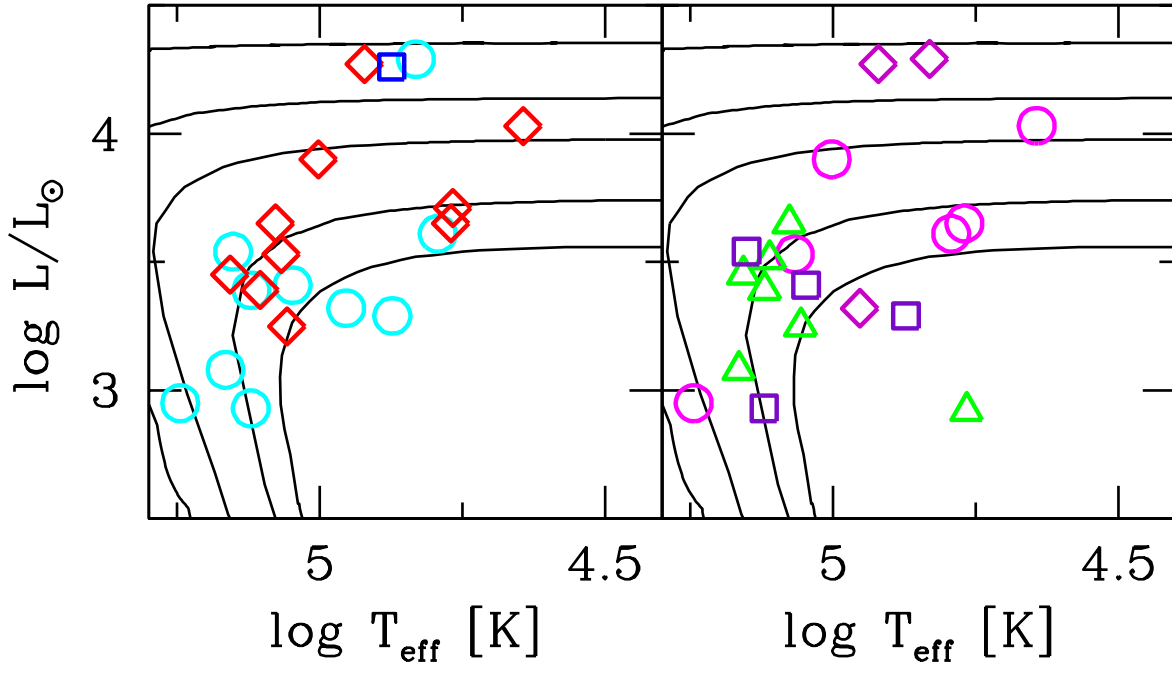


Fig. 14.— The loci of the central stars of a subsample of the studied PNe on the HR plane. Symbols of the observed PNe are as in Fig. 9.

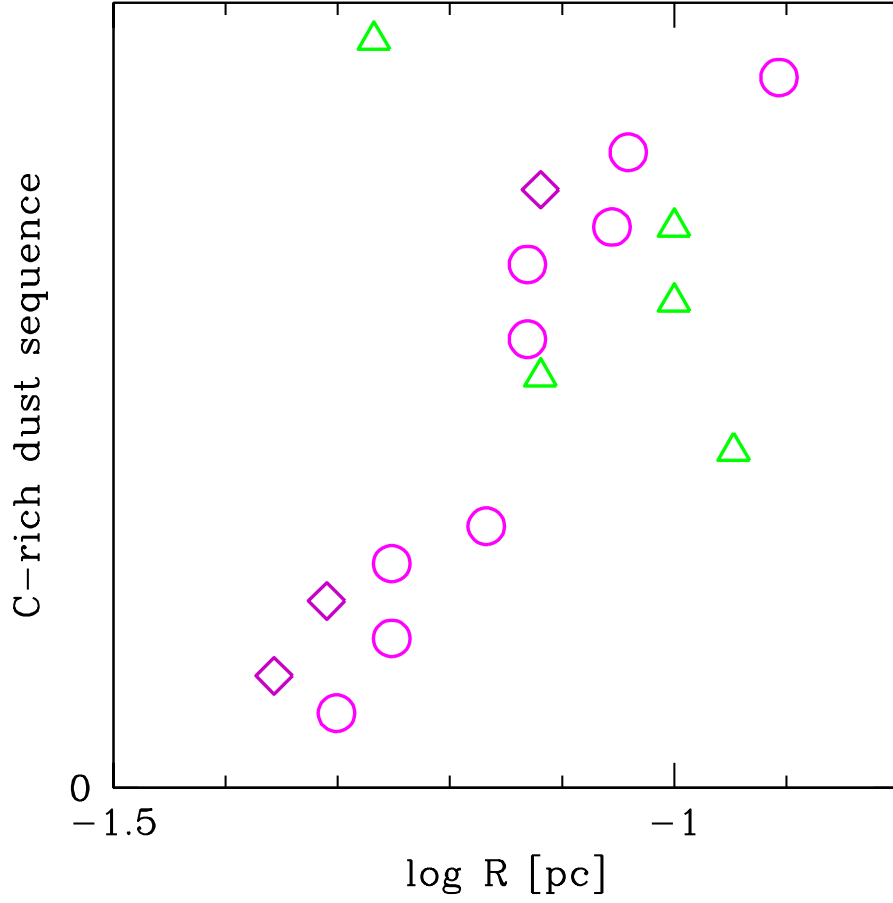


Fig. 15.— Schematic evolutionary sequence of CRD PNe, where we plotted the order of apparent evolution of the carbonaceous dust features, as in Figure 7a, b, and c, versus the photometric radii of the nebulae. Circles are round PNe, diamonds are elliptical PNe, and triangles are bipolar core PNe.